



# CHORUS

This is the accepted manuscript made available via CHORUS. The article has been published as:

## Modal interactions between a large-wavelength inclined interface and small-wavelength multimode perturbations in a Richtmyer-Meshkov instability

Jacob A. McFarland, David Reilly, Wolfgang Black, Jeffrey A. Greenough, and Devesh Ranjan

Phys. Rev. E **92**, 013023 — Published 30 July 2015

DOI: [10.1103/PhysRevE.92.013023](https://doi.org/10.1103/PhysRevE.92.013023)

**Modal interactions between a large wavelength inclined interface  
and small wavelength multimode perturbations in a  
Richtmyer-Meshkov instability**

Jacob A. McFarland,<sup>1,\*</sup> David Reilly,<sup>2</sup> Wolfgang  
Black,<sup>1</sup> Jeffrey A. Greenough,<sup>3</sup> and Devesh Ranjan<sup>2</sup>

<sup>1</sup>*University of Missouri Department of Mechanical and Aerospace Engineering,  
E2412 Lafferre Hall, Columbia, MO 65211*

<sup>2</sup>*Georgia Institute of Technology, George W. Woodruff School of Mechanical Engineering,  
801 Ferst Drive, Atlanta, GA 30332-0405*

<sup>3</sup>*Lawrence Livermore National Laboratory,  
7000 East Ave. PO Box 808, L-95 Livermore, CA 94550*

## Abstract

The interaction of a small wavelength multimodal perturbation with a large wavelength inclined interface perturbation is investigated for the reshocked Richtmyer-Meshkov instability using 3D simulations. The Ares code, developed at Lawrence Livermore National Laboratory, was used for these simulations and a detailed comparison of simulation results and experiments performed in the Georgia Tech Shock Tube facility is presented first for code validation. Simulation results are presented for four cases which vary in large wavelength perturbation amplitude and the presence of secondary small wavelength multimode perturbations. Previously developed measures of mixing, and turbulence quantities are presented which highlight the large variation in perturbation length scales created by the inclined interface and the multimode complex perturbation. New measures are developed for entrainment, and turbulence anisotropy which help to identify the effects of and competition between each perturbations type. It is shown through multiple measures that before reshock the flow processes a distinct memory of the initial conditions which is present in both large-scale-driven entrainment measures and small-scale-driven mixing measures. After reshock the flow develops to a turbulent like state which retains a memory of high amplitude but not low amplitude large wavelength perturbations. It is also shown that the high amplitude large wavelength perturbation is capable of producing small scale mixing and turbulent features similar to the small wavelength multimode perturbations.

PACS numbers: 47.40.Nm 47.20.Ma 47.27.Cn 47.20.Ft

---

\* mcfarlandja@missouri.edu

# I. INTRODUCTION

## A. Background

The Richtmyer-Meshkov (RM) instability is a hydrodynamic instability resulting from the interaction of an impulsive acceleration and a misaligned density gradient. The impulsive acceleration creates a pressure gradient in the form of a shock or blast wave, which propagates through a perturbed interface of a density gradient and imparts vorticity. The dependence upon the misalignment can be seen in the baroclinic term of the compressible vorticity equation 1.

$$\frac{D\vec{\omega}}{Dt} = \vec{\omega} \cdot \vec{\nabla} \vec{u} + \nu \nabla^2 \vec{\omega} + \left[ \frac{1}{\rho^2} \vec{\nabla} \rho \times \vec{\nabla} P \right]_{\text{baroclinic term}}. \quad (1)$$

Where  $\frac{D\vec{\omega}}{Dt}$ ,  $\vec{\omega}$ ,  $u$ ,  $\nu$ ,  $\rho$ , and  $P$  are the material derivative of vorticity, vorticity, velocity vector, kinematic viscosity, density, and pressure, respectively. It can be seen in equation /refe1 that the baroclinic term houses both pressure and density gradients, and the physical misalignment of these terms is represented by their cross product. The vorticity deposited at the interface stretches the surface area between the two fluids and rapidly increases the mixing as well as the diffusion across the now larger area. The amount of vorticity deposited is directly related to the strength of the pressure and density gradients. The strength of the pressure gradient is represented by the Mach number; the larger the Mach number the more vorticity is deposited on the interface. The density gradient strength is related to the Atwood number (eqn. 2), a non-dimensionalized parameter comparing the densities. In equation 2 the subscripts  $l$  and  $h$  refer to the densities of the light and heavy fluids respectively.

$$A = \frac{\rho_h - \rho_l}{\rho_h + \rho_l}. \quad (2)$$

As previously discussed, three main ingredients are necessary for the RM instability: an impulsive acceleration, a density gradient, and misalignment between the two. Through the history of RM research, perturbations in both the density gradient and the pressure gradient have been studied using various methods. Early work used a membrane to separate the two gases and while this method has significant disadvantages for optical diagnostics it is still employed successfully in many experiments today [1–3]. Fluid interface perturbations have been created by using gas-bubble interactions in which a bubble of density  $\rho_1$  was released into a shocktube filled with gas at  $\rho_2$  [4]. Another method used included dropping gas

cylinders into the shock tube which would create a double perturbation interface as the shock would travel from  $\rho_1$  to  $\rho_2$  and back to  $\rho_1$ , [5]. Both Motl *et al.* [6] and Krivets *et al.* [7] created a standing sinusoidal wave interface by oscillating the tube in an effort to create a well-characterize fluid perturbation. Just as the fluid perturbation has been researched, so too have various methods of creating the pressure gradient. Chapman and Jacobs [8] placed a test bed on a sled and accelerated the apparatus toward a spring near the end of the track while Robey *et al.* [9] applied a laser-driven shock wave. The most prevalent method of creating the shock wave is to mechanically generate it by the instantaneous release of high pressure gas into low pressure gas. The device which utilizes this method is known as a shock tube.

Just as the literature is rich with experimental studies, there are many simulations used to understand, qualify, and study the RM instability. Latini *et al.* [10] explored the RM instability of a single perturbation but continued the simulation to encompass reshock at late time, where the shockwave returns after being reflected by the back wall of the computational domain and utilized a weighted 9th order weight essentially nonoscillatory (WENO) shock-capturing method to simulate the physics. Peng *et al.* [11] studied the growth rate of a single perturbation diffuse interface using 2D Euler simulations and identified late time vortex accelerated secondary vorticity deposition. Lombardini *et al.* [12] studied the transition of a single shock RM instability to a turbulent state using 3D Large-Eddy simulations (LES) with a hybrid WENO-tuned-center-difference scheme and the stretched vortex subgrid scale (SGS) model. These simulations used a relatively low resolution, 128 nodes per largest wave length, but resolved a  $K^{-5/3}$  power law decay in the turbulent kinetic energy (TKE) spectra for shock wave Mach numbers over 1.5. Grinstein *et al.* [13] performed 3D simulations of a single shock RM instability of a multimode interface using the RAGE code which employed an ILES method with a second-order Godunov-type scheme and adaptive mesh refinement (AMR), similar to the Ares code used in this work. These simulations used a maximum resolution of approximately 24 nodes per large wavelength and resolved a  $K^{-5/3}$  power law decay in the TKE spectra over less than a decade of scales. These previously discussed methods of disturbing the fluid interface are all examples of single mode perturbations. Much research has explored the realm of multimodal perturbations of the interface in both experiments and simulations. Olsen and Greenough [14] considered 2D and 3D simulations for both single and multimodal perturbations and found that often the 2D under-predicts the

mixed mass. Miles *et al.* [15] performed simulations which studied the effect of multimodal perturbations combined with laser driven blast waves towards the goal of understanding the growth of the highly turbulent mixing layers in supernovae.

In recent years the RM instability has been increasingly studied for its applications in many areas. It has applications in astrophysics where its inclusion increases accuracy when modeling the behavior of super novae [16]. Inertial Confinement Fusion (ICF) is another area where RM research is focused. ICF involves a shock wave penetrating several layers of different densities with perturbations in each layer. These layers experience both the RM instability and the Rayleigh-Taylor instability [17, 18]. ICF is of great focus and interest to RM researchers as it has the potential to generate a substantial amount of energy while significantly reducing CO<sub>2</sub> emissions.

The inclined interface perturbation is employed in this study for the large wavelength perturbation. This perturbation allows for precise control of the vorticity deposition by changing the cross product between the density and pressure gradients across the entire interface. It is also a simple and highly repeatable interface perturbation which is subject to very little run-to-run variation [19]. This perturbation can be coupled easily with more traditional sine-wave type perturbations or complex multimode perturbations. Recently, several experiments have employed a sheared Kelvin-Helmholtz (KH) type interface to develop a complex multimode perturbation which is statistically repeatable [20, 21]. This type of interface creates a range of perturbation wavelengths and amplitudes as well as a larger diffusion thickness and a complex stratification created by KH vortices. This type of complex perturbation has been coupled with the inclined interface perturbation in experiments being performed in the Georgia Tech Shock Tube facility (fig. 1). The combination of these perturbation methods makes it possible to study the effect of large wavelength perturbations on the late time turbulent flow field and to explore the prevailing hypothesis that a memory of large wavelength small amplitude perturbations persists in shock-driven variable-density flows even at late times where the flow field has become more turbulent.

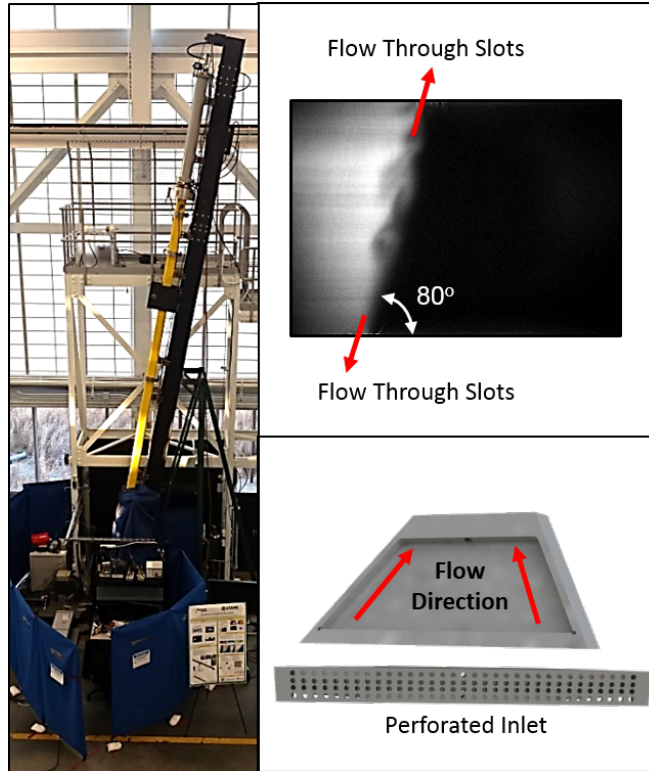


FIG. 1. (Color Online) Experimental facility. Left: The Georgia Tech Shock Tube facility inclined at  $80^\circ$ . Top Right: A sample image of the experimental multimode complex stratified perturbation. Bottom Right: The suction slot filler used to create the interface..

## B. Experimental description

The simulation conditions used in this paper were chosen to match the experimental conditions employed in the Georgia Tech Inclined Shock Tube facility (fig. 1, left). Experimental results will be presented in the following sections for simulation validation and so a limited discussion of the experimental apparatus and techniques is presented. Interested readers should refer to the publications which focus on the experimental work for a more experiment details [19, 22]. The shock tube employs a variable inclination design to create a stably stratified membraneless interface inclined with respect to the incident shock front. The driven and test sections can be rearranged to create different experimental conditions and to image the interface at different times. The membraneless interface is created by continuously flowing pure gases into the tube and exhausting the diffused gases at the interface to the atmosphere through slots in the shock tube walls. The flow of these gases is controlled by solenoid valves which shut before the incident shock reaches the interface. The effect of these slots on the flow field is mitigated by employing a porous surface (fig. 1) to reduce the flow rate of high pressure post shock gas into the slot volume. The suction slot volume is also minimized to reduce the total amount of post shock gas which may enter them. This facility is designed to run many experiments in a short time (20-30 per day) in order to achieve statistically converged results.

Particle imaging velocimetry (PIV) and planar laser induced fluorescence (PLIF) of acetone are used to measure velocity fields and approximate species concentrations. PIV measurements are made using a 200mj/pulse 532nm NdYAG laser, and TSI Inc. PowerView Plus 2MP cameras. The gases are seeded with glycerin particles which have a mean diameter of  $0.2 \mu\text{m}$  and vectors are calculated using the TSI Insight4G software. More details are presented in the previous experimental work [22]. PLIF images are acquired using a 60mj/pulse 266nm NdYAG laser and a TSI PowerView 29MP camera with 4x4 pixel binning. The acetone is seeded in the light gas using a custom acetone seeder with an approximate concentration of 6% by volume. The low acetone concentration and pixel binning allows for low laser extinction through the inclined interface which is particularly susceptible to light extinction problems due to its large interface mixing width.

### C. Simulation description

The computation study was performed using the Ares code, a staggered mesh arbitrary Lagrange Eulerian (ALE) hydrodynamics code developed at Lawrence Livermore National Laboratory. The Lagrange time advancement is second-order predictor- corrector and uses the Gauss Divergence theorem to give the discrete finite difference equations [23]. All numerical differences are fully second order in space. Velocities are defined at mesh nodes and density and internal energy are defined at the zone centers using piecewise constant profiles. Artificial viscosity is used to suppress spurious oscillations [24]. A second-order remap [25] is applied to the solution after the Lagrange step. In these simulations, a fixed Eulerian mesh is used at all times. The Ares code includes an adaptive mesh refinement (AMR) capability that allows the base resolution to be increased by a factor of three for each level of refinement. The refinement is performed on areas that exceed an error tolerance in the computation of a second undivided difference of pressure and on all mixed zones. The AMR approach implemented in Ares follows that of Berger and Olinger [26] and Berger and Colella [27]. Time advancement is not recursive though, and the coarser levels are slaved to run at the finest level time step. This approach has been extensively studied and provides a factor of 57 increase in efficiency over a fully refined everywhere simulation.

The Ares code solves the Navier-Stokes equations for multi-species flows, conservation of mass, momentum, and energy, shown in equations 3 - 5 where  $Y_n$  (eqn. 11) is the mass fraction of species  $n$  and  $\rho$  is the mixture density. These equation are given in Einstein notation where the super/subscripts  $i, j$ , and  $k$  denote direction indices, and  $m$  and  $n$  denote species indices. Summation is implied between superscripts and subscripts with repeated indices and Hadamard products (element-wise product) are implied by repeated superscripts or repeated subscripts.

$$\frac{\partial \rho Y_n}{\partial t} + \partial_i (\rho Y_n u^i + \varphi_n^i) = 0. \quad (3)$$

$$\frac{\partial \rho u_j}{\partial t} + \partial_i (\rho u^i u_j - T_j^i) = 0. \quad (4)$$

$$\partial_t (\rho e) + u^i \partial_i (\rho e) + P \partial_i u^i + \partial_i q^i - T_j^i \partial_i u^j = 0. \quad (5)$$

The mass flux,  $\varphi_n^i$ , stress tensor,  $T_j^i$ , and specific internal energy,  $e$ , are given in equations 6-8 where  $\delta_j^i$  is the Kronecker delta operator,  $\mu$  is the mixture viscosity (eqn. 14), and  $e_m$  is the internal energy of species  $m$ . The energy flux,  $q_i$ , is given in equation 9. Ares correctly accounts for energy changes due to mixing [28]. The strain rate tensor,  $S_j^i$ , is given in equation ten.

$$\varphi_n^i = -\rho(D_n \partial^i Y_n - Y_n D^m \partial_i Y_m). \quad (6)$$

$$T_j^i = -P \delta_j^i - \frac{2}{3} \mu \partial^k u_k \delta_j^i + 2\mu S_j^i. \quad (7)$$

$$e = Y_m e^m. \quad (8)$$

$$q^i = -\kappa \partial_i T + h_n \varphi_i^n. \quad (9)$$

$$S_j^i = \frac{1}{2} (\partial^i u_j + \partial^j u_i). \quad (10)$$

Taking the partial volume approach where  $V$  ( ) is the mixture volume (density) and  $V_m$  ( $m$ ) is the species partial volume (density), the mass fraction and volume fraction are described in equations 11 and 12. The species partial pressure,  $P_m$ , and mixture velocity,  $u_i$ , are given in equations 13 and 14. The ideal gas equation of state (eqn. 15) was used for the species  $N_2$  and  $CO_2$  to close the equations, where  $R$  is the gas constant defined in equation 16,  $M$  is the species molecular weight, and  $r$  is the universal gas constant 8.314 kJ/kmol-K. The internal energy and enthalpy ( $h_n$ ) are found using the ideal gas form shown in equations 17 and 18, where  $\gamma$  is the ratio of specific heats.

$$Y_m = \frac{\rho_m}{\rho}. \quad (11)$$

$$x_m = \frac{V_m}{V}. \quad (12)$$

$$P = x_m P^m. \quad (13)$$

$$u_i = y_m u_i^m. \quad (14)$$

$$P^m = \rho^m R^m T. \quad (15)$$

$$R^m = \frac{r}{M^m}. \quad (16)$$

$$e^m = \frac{rT}{M^m(\gamma^m - 1)}. \quad (17)$$

$$h_n = e_n + \frac{P_n}{\rho_n}. \quad (18)$$

Molecular viscosity and diffusion models developed and described in previous work [29, 30] were implemented. The viscosity model is temperature dependent based on the Sutherland law for ideal gases (eqn. 19), and mixed zone viscosities are calculated using the volume fraction,  $x^m$  (eqn. 20). The molecular diffusion coefficient follows the empirical correlation given by Gilliland [31] shown in equations 21 and 22 where the index notation  $m + 1$  is cyclical (i.e., for  $m = 2$ ,  $m + 1 = 1$ ). The coefficients  $n$  are given by Poling *et al.* [32]. The constants for the viscosity and diffusion models are summarized in table I along with the ratio of specific heats  $\gamma$ .

$$\mu_m = \alpha_m \frac{T^{1.5}}{B_m + T}. \quad (19)$$

$$\mu = x^m \mu_m. \quad (20)$$

$$D_m = \frac{c_m T^{1.5}}{P}. \quad (21)$$

$$c_m = \frac{435.7}{\left(\epsilon_m^{1/3} + \epsilon_{m+1}^{1/3}\right)} \left(\frac{1}{M_m} + \frac{1}{M_{m+1}}\right)^{1/2}. \quad (22)$$

Boundary conditions were explored in 2D simulations described in the following section, but for the 3D simulations presented in this paper all boundaries were no penetration, shock reflecting which allowed slip. The computational domain was 11.43 cm in the Y direction

TABLE I. Coefficients for viscosity and diffusion models

Gas	$\alpha$ ( $g/(cm \mu s K^{1/2})$ )	$B(K)$	$\epsilon$	$M(mol/g)$	$\gamma$
$N_2$	$1.407 * 10^{11}$	111.0	18.5	28.013	1.4
$CO_2$	$1.572 * 10^{11}$	240.0	26.9	44.01	1.28

(fig. 2), and 251.46 cm in the X direction (X-Y aspect ratio of 22). The selection of the Z direction distance in 3D simulations is discussed in detail later but was set to 2.286 cm deep (Y-Z aspect ratio 5). The upstream boundary contained a source term to sustain the shock front which supplied mass and the post shock conditions at all times. The interface was prescribed with a base inclined perturbation in the X-Y plane between the  $N_2$  and  $CO_2$ . In an effort to use the familiar language of sine-wave type perturbations, the X-dimension height of the inclined perturbation will be referred to as the amplitude while its wavelength will be defined as twice the Y dimension (see [29] for details). The interface is set up with an initially diffuse layer prescribed by an error function based on experimental measurements (see [30] for more details) with a set thickness of 1.2 cm for most cases. The choice of this diffusion thickness was based on initial PLIF images of the experimental interface which showed a 1-99% species mass fraction based diffusion thickness of 1 to 1.4 cm. A 2D simulation study of the diffusion thickness also showed the best agreement with late time experimental images using a thickness of 1.2 cm. A multimode perturbation was applied to this base inclination using a coordinate transfer to the W-V plane. 3D perturbations were applied using an inclination in the V-Z plane coupled with a multimode perturbation. Details on the design of these perturbation are given in the later sections. The shock is initialized 2 cm ahead of the interface as a region of  $N_2$  at post shock conditions. Additional source terms were used to model mass loss through the suction slots in the experiments and are discussed in the following section.

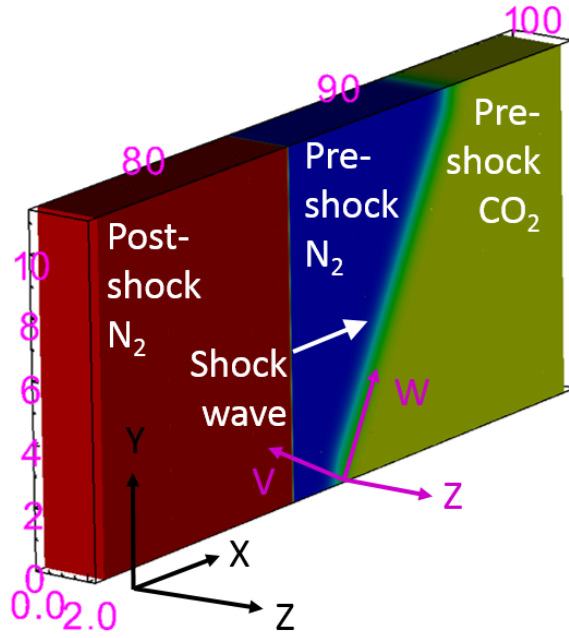


FIG. 2. (Color Online) Section of computational domain showing initialization of the interface and shock wave and coordinate system. The full domain Y and Z dimensions are shown. The X dimension is shown from 75 to 100 cm. The full domain extends from 0 to 251.46 cm in the X dimension.

## II. COMPARISON TO EXPERIMENTS

The simulation results were first compared with experiments to improve the simulation-experiment agreement and to examine the factors which contribute most to their disagreement. In this process experimental results were compared with 2D and 3D simulation results and modifications were made to the boundary conditions, resolution, and initial conditions. Below a brief description of the experimental results will be presented followed by an examination of simulation parameters in a 2D study with a comparison to experiments. The section will conclude with the extension of the 2D parameter study results to a 3D simulation and a comparison to experiments which shows improved agreement.

### A. Experimental results

The base case for comparison between the experiments and simulations was a  $60^\circ$  interface with  $N_2$  over  $CO_2$  ( $A$  0.23) which is accelerated by a Mach 1.55 incident shock wave. A time series of the experimental interface evolution was obtained with the PLIF diagnostic and is shown below in figure 3. At early times the development of two large vortices can be seen. At 4.91 ms after incident shock acceleration the interface shows a large primary vortex at the upstream edge and a smaller secondary vortex created from the merger of two small vortices. The primary vortex shows the evolution of secondary vortices seeded by shear at the outer most edge of the primary vortex which then become Rayleigh-Taylor unstable and grow due to the centripetal acceleration of the vortex [10] (fig. 4). PIV measurements of the 2D velocity and vorticity field have also been obtained for these experiments and show qualitative agreement with the PLIF measurements (fig. 4). These measurements will be used in the following sections for comparison to simulation data.

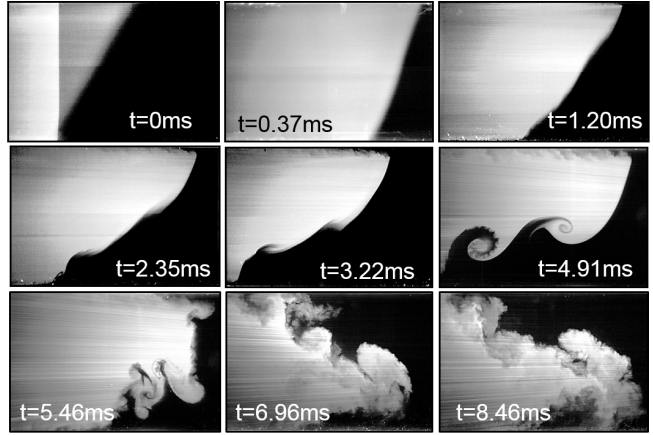


FIG. 3. Time series of experimental PLIF images showing the evolution of the  $60^\circ$  inclined interface through reshock.

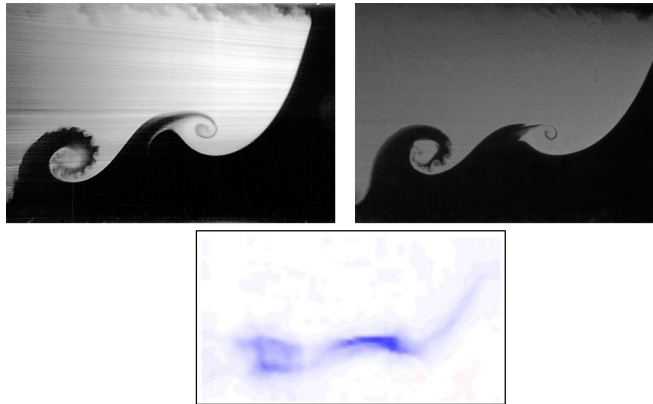


FIG. 4. (Color Online) Comparison of PLIF image, Mie scattering image, and PIV vorticity field. Top left: PLIF image at 4.9 ms. Top right: Mie scattering image at 5.1 ms. Bottom: vorticity field from PIV measurements at 5. ms.

## B. 2D simulation results

In an effort to match the experimental and simulation initial conditions better and improve qualitative agreement, a 2D simulation parameter study was undertaken. Previous simulations deviated from experiments in that the second and third vortices did not merge, the interface velocity was slower, and that secondary vortex-accelerated vortices did not develop on the primary vortex. In order to improve agreement with the experimental results several parameters, the initial interface perturbation, simulation resolution, and boundary conditions, were systemically varied. This parametric study provided useful insights on the effects of these parameters on the developing flow field. The 2D simulations were run with a computational domain as described in the introduction excluding the  $Z$  dimension. The resolution at the highest AMR level for the base simulations was  $283 \mu\text{m}$  or 810 nodes per wavelength. The first parameter explored was the interface perturbation. The experimental interface deviates from the ideal planar case in part due to the orientation of the slots in the shock tube wall (see section I B). These slots cause the interface to align normal to the shock tube walls as the flow exits. A multimode perturbation is applied on top of the inclined interface consisting of a Fourier series. This Fourier series was developed from both experimental Mie scattering and PLIF images of the interface just prior to shock interaction ( $< 100\mu\text{s}$ ). The small amplitude modes in these images varied from run to run and between visualization techniques. The large modes which accounted for the curving of the interface near the suction slots did not. The simulations were found to be sensitive to the small mode perturbations near the center of the interface and diminished the agreement with experiments. To rectify this an artificial set of modes was constructed which accounted for the edge curvature but had no small modes in the center of the interface (fig. 5). This multimode perturbation was tested in the 2D simulations and a qualitative comparison of the late time (5.1ms) species field showed modest improvement in vortex position and merging.

The next parameter explored in the 2D simulations was the maximum resolution used. The base simulations used four levels of refinement which provided for a maximum resolution of  $283 \mu\text{m}$ , or 810 nodes per wavelength. A qualitative resolution study was run with four different resolutions (11, 33, 47,  $283 \mu\text{m}$ ) where the maximum resolution was increased to  $11 \mu\text{m}$ , or 21,870 nodes per wavelength. At a resolution of approximately  $47 \mu\text{m}$  the secondary vortices became apparent on the primary vortex (fig. 6). Quantitative measures such as the

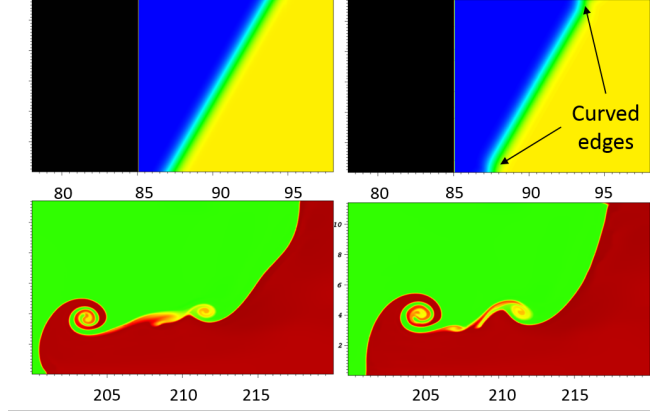


FIG. 5. (Color Online) Density plots of the initial condition (top) and 5.1ms (bottom) flow field for the pure inclined interface (left) and the artificial multimode construction of the interface (right).

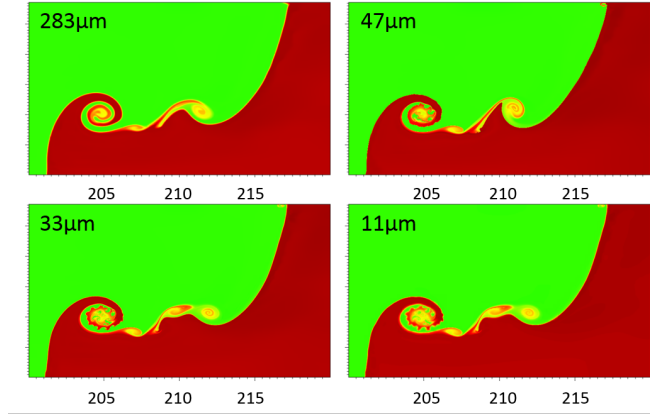


FIG. 6. (Color Online) Density plots of the flow field at 5.1 ms for different maximum resolutions.

amount of total positive circulation showed that this secondary vorticity began effecting the results starting at 3 ms and created a total deviation in positive and negative circulations of about 15

After determining the appropriate simulation resolution the boundary conditions effects were explored. Previous simulation work on this problem used a no-slip boundary to develop boundary layers. Due to resolution limitations ( 283  $\mu\text{m}$ ) in this work the boundary layers were not fully developed and grew as laminar layers. As higher resolutions were explored it was observed that at a resolution of 33  $\mu\text{m}$  the boundary layers grew larger and appear more turbulent (fig. 7). The effects of the boundary layers then began to propagate further into the core of the flow increasing the circulation. It was also observed that the boundary layers

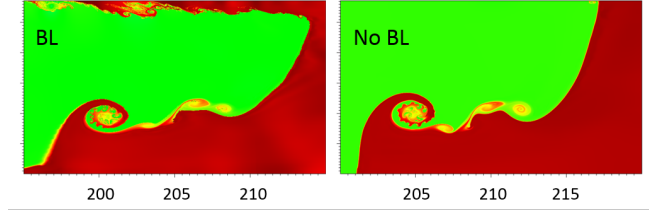


FIG. 7. (Color Online) Density plots of the flow field at 5.1 ms for the case with boundary layers (left) and without (right).

slowed the interface velocity but had little effect on the growth of the core mixing region. This result is different from the boundary layer effects observed for small wavelength, low amplitude perturbations where the walls were far away from the growing perturbations (1.5 to 2.5 wavelengths per boundary pair) [33]. While the inclined interface perturbation is coupled with the boundary layers (0.5 wavelengths per boundary pair) the growth rate of the large wavelength high amplitude perturbation was found to be insensitive to the boundary layer development especially at higher Mach numbers. Since the boundary layers slowed the interface velocity compared to experiments and had no effect on the growth rate, they were removed from further simulations. This also saved considerable time since the AMR tagged the boundary layers to the highest level which increased the total number of nodes in the domain by a factor of up to five.

Another important boundary effect is that of the interface slots. These slots are blocked by a valve on the outside of the tube but have a small volume which allows some mass to exit the experimental domain as the shock wave compresses the interface. To diminish this effect in the experiments the slots used a porous surface which mostly reflected the incident shock, reduced the slot volume, and diminished the flow rate of mass into the slot volume. In an attempt to model the slot effects, a source term which pulled mass from the interface at a rate proportional to the slot open area and the post shock 1D gas dynamics velocity was added. This source was also slightly delayed so that it did not occur until after the shock wave had fully crossed the slot. The upper boundary slot has the most potential to affect the development of the interface since the interface is nearest this slot when the source is activated. Modeling the upper slot alone improved the vortex merging (fig. 8). The lower wall slot has a smaller effect since it is delayed until after the incident shock passage, but when it was applied it reduced the qualitative agreement. The reason

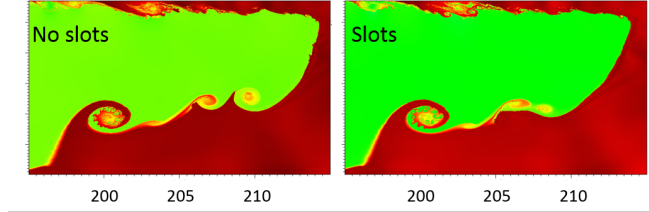


FIG. 8. (Color Online) Density plots of the flow field at 5.1 ms for the case without slot effects modeled (left) and with the top slot effects modeled (right).

for this is likely that the mass does not exit at the rate or at the time it was estimated to in the simulation. Without further measurements of the slot effects in the experiments it is impossible to diagnose this effect better and so only the top slot was modeled in further simulations since only qualitative agreement was sought.

### C. 3D simulation comparison

Based on the results of the 2D simulations a 3D problem was created for comparison with the experiments. The need for 3D simulations was primarily driven by the need to explore modes in the Z dimension which might create significant features after reshock. In the section below it will be shown that the circulation deviated between the 2D and 3D cases by a modest amount after reshock. For the development of the complex multimode perturbation discussed later though, 3D simulations were required since the complex perturbation is highly three dimensional and creates significant growth in the Z direction. To approximate the experimental initial conditions in the Z direction Mie scattering images were acquired of the experiment in the Y-Z plane at several X locations throughout the interface (fig. 9). The images were processed to find a modal description of the Z direction perturbation. Each location showed a low amplitude noise coupled with a slight inclination of  $0.1^\circ$  in the V-Z plane. This inclination was likely due to a slight deviation in the shock tube foundation. For the 3D simulation a random noise consisting of 50 modes with similar amplitudes and wavelengths to the experimental noise were used. The amplitude of these modes was low compared to the inclined interface amplitude and they are plotted in wave space at the top of figure 9. These accurately replicated the bounds of the noise found in the ensemble of experimental images. The  $0.1^\circ$  inclination was also applied in the simulations.

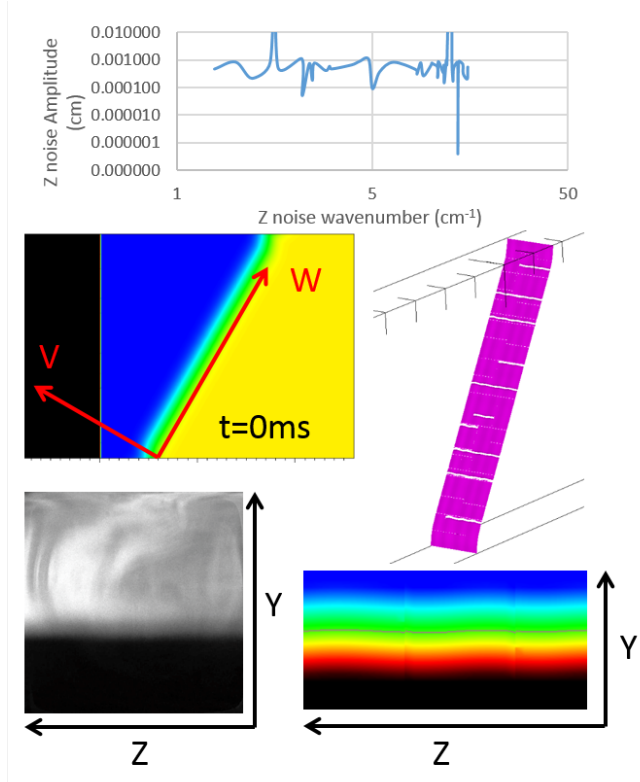


FIG. 9. (Color Online) Experimental and simulation images of the initial conditions. Top: Z noise perturbation mode amplitudes versus wave number. Middle left: 2D pseudocolor X-Y slice of the simulation density field, Middle right: 3D countour of the simulation 50%  $N_2$  mass fraction, Bottom right: 2D pseudocolor Z-Y slice of the simulation density field where the magenta line indicate the 50% contour of species fraction, Bottom left: Experimental Mie scattering image of the Z-Y plane of the initial conditions.

Figure 9 shows the simulation initial conditions and a sample experimental image of the Z perturbation.

Even with AMR extending the computation domain into the Z dimension presented significant problems with computational resource limits. For this reason it was desirable to limit the Z dimension of the computation domain. The experimental images of the interface suggested that the perturbation was largely contained in the X-Y plane with perturbations in Z direction consisting of noise with wavelengths less than 1 cm. Therefore, to enhance the computational speed, rather than simulating the whole Z-dimension (11.43 cm), the problem was limited to 1/5 of the full Z-dimension (2.286 cm). To study the effect of this limit several lower resolution ( $\sim 423 \mu m$ ) simulations were run with varying Z dimensions from one to

one tenth of the experimental dimension. This study showed no variation in quantitative measures of mixing, circulation or TKE. With the Z dimension selected, a resolution study was undertaken to find the maximum resolution that could be run with the computational resources available (512 processors, 2 GB memory per processor). It was determined that the maximum resolution which could be achieved was  $141 \mu\text{m}$ , or 1,620 nodes per wavelength. This resolution was a factor of three greater than the  $47 \mu\text{m}$  resolution found to reproduce the secondary vortex-accelerated vorticity. This, unfortunately, was a necessary sacrifice. With AMR and a maximum resolution of  $141 \mu\text{m}$  the simulations reached in excess of 200 million nodes at post reshock times.

Figure 10 shows 3D contours of the species mass fraction at various times in the simulation interface evolution. It is apparent at early times that a small amplitude and wavelength Z perturbation has grown but its amplitude remains insignificant compared to the X-Y plane inclined perturbation. After reshock (bottom fig. 10) the Z perturbation has become more complex. Figure 11 highlights the Z perturbation after reshock and shows X-Y plane slices of density from three different Z coordinates compared to the late-time species contour. The Z perturbation can be seen to consist mostly of small modes with the large structures remaining coherent across the Z direction. The primary vortex has become well mixed with large amounts of mass penetrating the interface. Figure 12 shows 2D center slices of the density field compared to experimental PLIF images. At early times, the two vortices show similar positions and developments. Just prior to reshock the simulation and experiment both show a well-developed primary vortex with a second strong vortex at the center of the interface which resulted from the merger of two smaller vortices. In addition, a fourth small vortex is visible behind the primary vortex in the simulation and just above the second large vortex in the experiment. While the position and merger of the second vortex agrees well, there is a larger accumulation of mass at the second vortex in the experiments due to the position of the fourth small vortex which is merging with the larger second vortex. The primary vortex also remains less diffused in the simulation whereas in the experiments it becomes hard to see as the  $\text{CO}_2$  is pulled inward. The overall position and length of the interface agrees well. After reshock the several large scale features are similar including the bubble location and the reshock spike growth, but many of the smaller features are not similar. Most notably the spike exhibits a fork in the experiments but not in the simulations. This may be a boundary layer effect and will be explored in future simulations

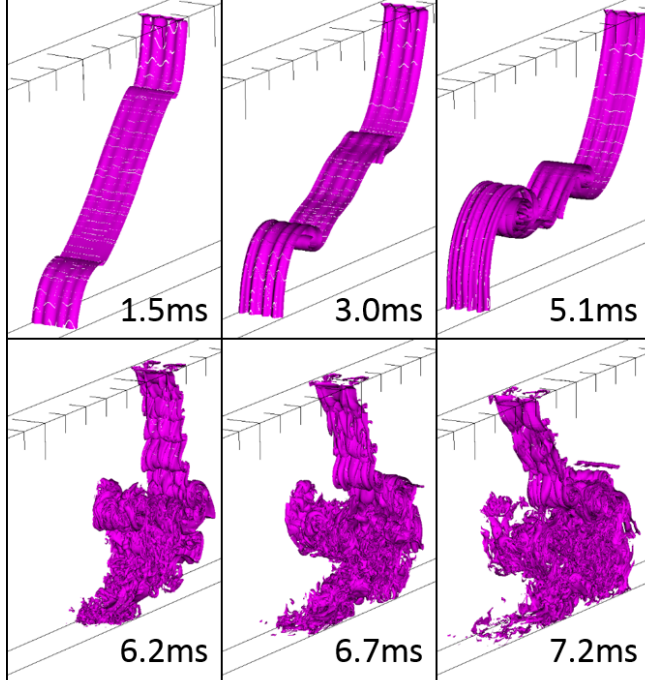


FIG. 10. (Color Online) Time series of species 50% mass fraction contours for the 3D simulations.

as the computational power to simulate the boundary layer becomes available.

Figure 13 shows integral mixing width (eqn. 23) for the simulation and experiments obtained using PLIF images. For the experimental measurements species fractions were inferred from acetone fluorescence levels. The boundary layers were also excluded by removing the upper and lower 5 mm of the image field which contained strong vorticity signifying the presence of the boundary layer. Overall, agreement is good, but mixing width is an integral measure which the 2D simulations also reproduced well. The positive, negative and total circulation are shown in figure 14 for the simulation and the experiment as defined in previous work [30]. Experimental vorticity measurements were obtained from PIV measurements reported on in previous work [22]. The circulation plot also shows good agreement with some disagreement in the negative circulation deposition after reshock. The circulation for 3D simulations differs from the 2D prediction by a maximum of 10% after reshock.

$$h = \int \langle Y_{N_2} \rangle \langle Y_{CO_2} \rangle dx. \quad (23)$$

The turbulent kinetic energy spectra was obtained from the simulation and experimental PIV data. For the simulation the AMR data was resampled at the highest resolution across

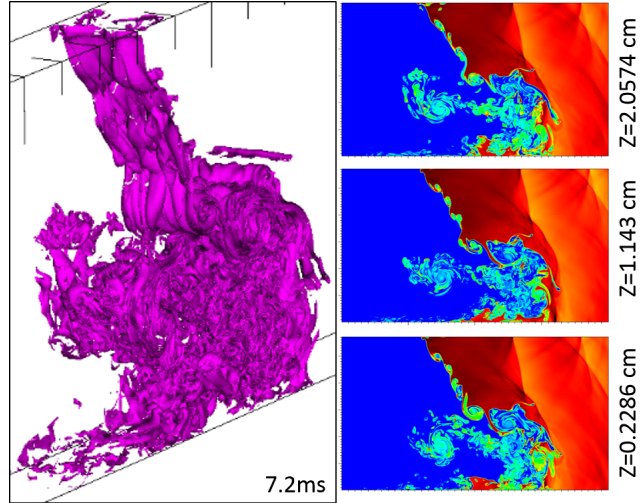


FIG. 11. (Color Online) Z perturbation after reshock ( $t=7.2\text{ms}$ ). Left: species 50% mass fraction contour. Right: X-Y plane slices of density plots at three Z locations; Top: 90% Z domain (2.0574 cm), Middle: 50% Z domain (1.143 cm), Bottom: 10% Z domain (0.2286 cm).

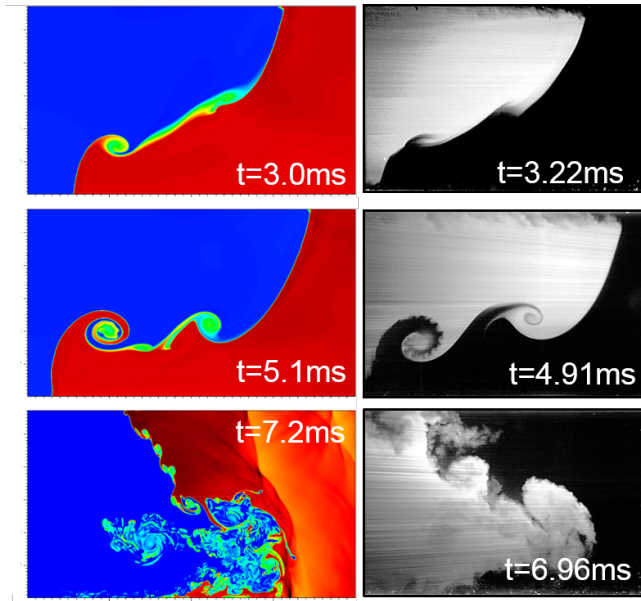


FIG. 12. (Color Online) Comparison of simulations and experiments. Left: center slices of density plots for the 3D simulations. Right: PLIF images of the experimental interface.

the mixing region. The fluctuating velocities were found and the 2D Fourier transforms taken across the Y-Z planes at each X location. The 2D Fourier spectra were averaged across the X dimension and then averaged across the Z or Y direction to find the TKE of

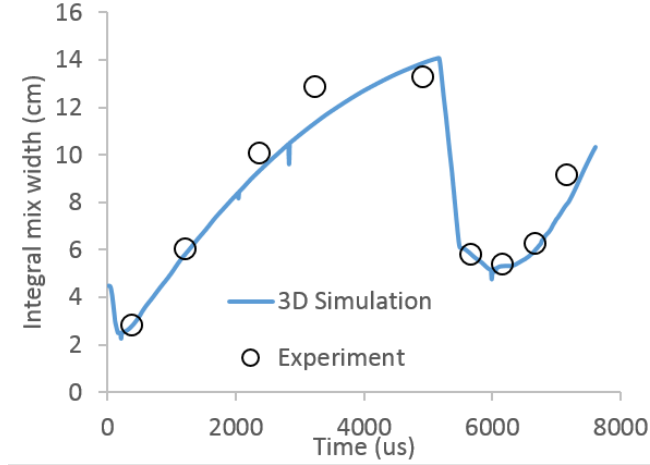


FIG. 13. (Color Online) Integral mixing width for the simulation and experiments.

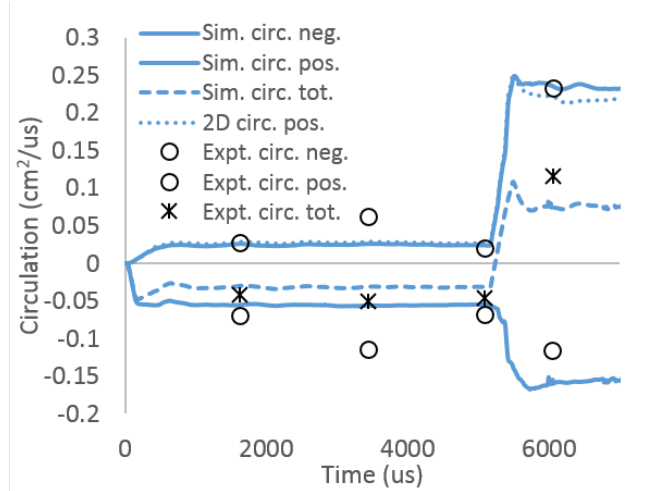


FIG. 14. (Color Online) Integral mixing width for the simulation and experiments.

the Y and Z wave numbers ( $K_y$  and  $K_z$ ), respectively. The TKE of the 2D radial wave number ( $K = \sqrt{K_y + K_z}$ ) was also found but is not presented since it is similar to the  $K_y$  spectra due to the 2D nature of the perturbation. The experimental data was limited to a 2D plane taken in the center of the tube and thus only the TKE of  $K_y$  could be found. The experimental data was ensemble averaged from 10 experiments. The resolution was 1.6 mm which limits the comparison to low wave numbers. Figure 15 shows the normalized TKE for the experiments and simulation. The TKE was normalized using the peak value for each case. Both the simulation and experiments exhibit an inertial range with an approximate  $K^{-5/3}$  trend after reshock. The simulation data however shows that the inertial range has

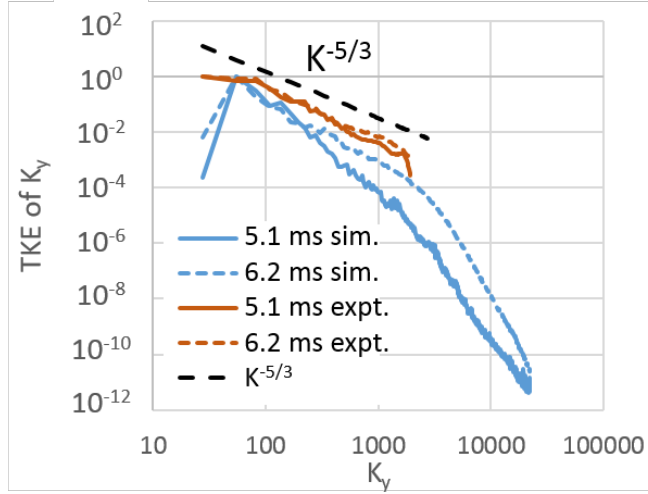


FIG. 15. (Color Online) Normalized turbulent kinetic energy spectra for the simulation and experiments.

not evolved prior to reshock whereas the experimental data shows an inertial range over at least one decade of length scales prior to reshock. It is expected that this trend would not continue to high wave numbers if this data was available from experiments.

### III. MODAL INTERACTION STUDY

Having shown the Ares code to be in good agreement with experimental results in the previous section its capabilities can be applied to study the interaction of the large wavelength inclined interface perturbation with a small wavelength multimode complex stratification perturbation such as arises in turbulent shear-driven interfaces. This study explores the effect of this complex multimode perturbation on the inclined interface with different amplitudes in 3D simulations to late time after reshock. The parameters were constrained to values which could be replicated in the Georgia Tech Inclined Shock Tube Facility to provide prediction of multimode experiments to be performed in the shock tube later. The following section will discuss the development of the initial conditions, and provide a qualitative and quantitative comparison which highlights the effects the base inclined interface amplitude and multimode complex stratified perturbation.

#### A. Initial conditions

All cases for this study will consist of an interface with  $N_2$  over  $CO_2$  with an incident shock wave Mach number of 1.55 into atmospheric pressure  $N_2$ . The cases are named in a descriptive manner where the number indicates the inclination angle, 6 for  $60^\circ$  and 8 for  $80^\circ$ , and the letter indicates the presence of the complex multimode perturbation, S for simple, no multimode perturbation, and M for multimode complex stratification perturbation. Figure shows the initial conditions for each case. The base case (6S) for this study will be the simulation discussed in the previous experimental comparison section which consists of a simple inclined interface perturbation at  $60^\circ$  with a small low amplitude multimodal contribution and simulated slot effects to match experimental conditions. For all other cases no attempt was made to model the slot effects or interface perturbation departure from the ideal case since no experiments have been conducted at these conditions for comparison. Case 8S consisted of another simple interface case with a low amplitude  $80^\circ$  inclined interface. Both case 6S and 8S used a 1.2 cm diffusion thickness similar to previous experiments (fig. 16). Case 6M and 8M contained a multimode complex stratification perturbation where case 8M has an underlying inclination of  $60^\circ$  and case 6M an  $80^\circ$  inclination. Table II summarizes the parameters for each case.

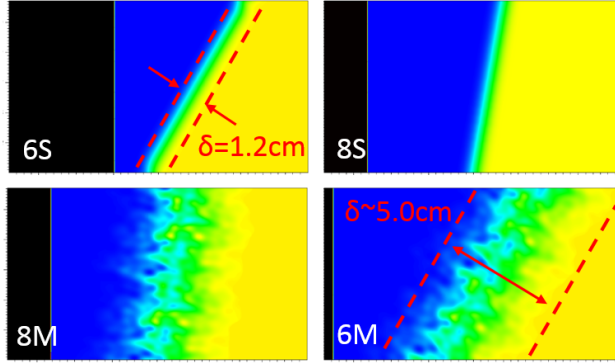


FIG. 16. (Color Online) Density plots of the initial conditions for each of the four cases.

TABLE II. Summary of the parameters for each simulation case

Name	Inclination	Perturbation
6S	60°	Experimental
8S	80°	None
8M	80°	Complex
6M	60°	Complex

The complex stratification was composed of a 2D multimode surface function and a 3D oscillating diffusion function which modified the species concentrations in the V direction. The base 2D surface perturbation was composed of 50 modes in the V-W and V-Z planes whose wavelengths were equally spaced between a minimum of 1 cm and a maximum of 11.6 cm, the maximum W dimension of the interface. The amplitudes and phases angles were randomly assigned between with bounds of 0 to 0.1 cm, and  $-\pi$  and  $\pi$ . The 3D oscillating diffusion function was an equally weighted combination of the error function diffusion layer used in the simple inclined interface and a 10-mode oscillating sine wave series which varied with V, W, and Z. The 10-mode oscillating series varied between zero and one as a function of V distance from the interface. The phase angle and amplitude of this function varied smoothly with W and Z. This oscillating function was coupled with an error function which diminished its effect as a function of the diffusion thickness and V distance from the interface. This complex stratification had an effective diffusion thickness of 5.0 cm (fig. 15) and created a complex stratification of gas species where it was possible

for the shock to enter and exit multiple layers of one species as it transited the interface. Equations 24-30 summarize the multimode complex stratification interface, and table III summarizes the variable ranges for these equations. Figure 17 shows the initial condition for the multimode complex stratification on an 80° inclination. The complex stratification varies more along the W direction similar to a shear interface. Variation in the Z direction is limited by the limited Z dimension. While this perturbation varies significantly in the Z direction, the overall coupled perturbation is driven mostly by the 2D inclined interface.

$$Y_1 = 0.5 * O(V_{dint}, W, Z) * erf(V_{dint}) + 1 - 0.5 * \left(1 + erf(V_{dint})\right). \quad (24)$$

$$V_{dint} = V - V_{int}(W, Z). \quad (25)$$

$$V_{int} = \sum_{i=1}^{50} A_o(i) * cos\left(W * K_o(i) + \Phi_o(i)\right) + A_p(i) * cos\left(W * K_p(i) + \Phi(i)\right). \quad (26)$$

$$O(V_{dint}, W, Z) = \sum_{i=1}^{10} A_r(i) * A_q(i) * cos\left(W * K_q(i) + \Phi_r(i)\right). \quad (27)$$

$$A_r(i) = sin\left(\frac{4\pi * W}{W_{max}} + \frac{4\pi * V}{W_{max}} + \Phi_q(i)\right). \quad (28)$$

$$\Phi_r(i) = 2\pi * A_r(i). \quad (29)$$

$$K_q = 2\pi/\lambda_q. \quad (30)$$

The 50% species contours and density plots at the center X-Y plane for the four simulations are shown below in figures 18 and 19 for three times, from immediately prior to reshock, to 2.1 ms after reshock. Before reshock the shape of the interface for each case is unique. Case 6S shows a well-developed primary and secondary vortex while case 8S only shows inflection points. Case 8M and 6M show a similar turbulent mixing region but have strongly differing large wavelength amplitudes. After reshock case 8S stands out as having particularly low mixing while cases 6S, 8M, and 6M exhibit similar amounts of small scale structures. For case 6S these small scale structures involved in mixing are concentrated in

TABLE III. Summary of variables for multimode complex stratification

Variable	Minimum value	Maximum value	Distribution
$W_{max}$	11.6 cm	11.6 cm	Constant
$\lambda_o, \lambda_p$	1 cm	11.6 cm	Even
$A_o, A_p$	0 cm	0.1 cm	Random
$\Phi_o, \Phi_p$	$-\pi$	$\pi$	Random
$\lambda_q$	1 cm	10 cm	Even
$A_q$	1 cm	5 cm	Even
$\Phi_q$	$-\pi$	$\pi$	Random

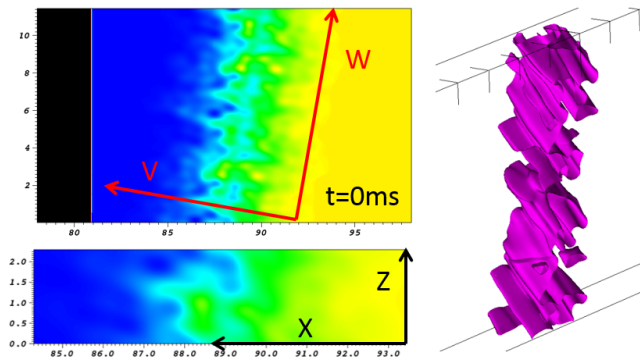


FIG. 17. (Color Online) Initial conditions for the multimode complex stratification at an  $80^\circ$  inclination. Top Left: Center slice in the X-Y plane of the density contour. Bottom Left: Center slice in the X-Z plane of the density contour. Right: 50% contour of the  $N_2$  mass fraction..

the lower left corner in the region which was the sight of the primary vortex before reshock. For case 8M and 6M the small scale structures are well distributed across the interface with case 6M exhibiting a slightly wider turbulent mixing region. Case 6S recovers an underlying large wavelength structure at late times which is similar in amplitude to case 8S while cases 8M and 6M have similar low amplitudes due to the damping from the large amount of turbulent mixing created. Figure 20 shows the distribution of vorticity in the center X-Y plane over time for each of the cases. From the vorticity plots it can be seen that case 6S and 8S both possess a positive vortex sheet after reshock which is similar in strength and

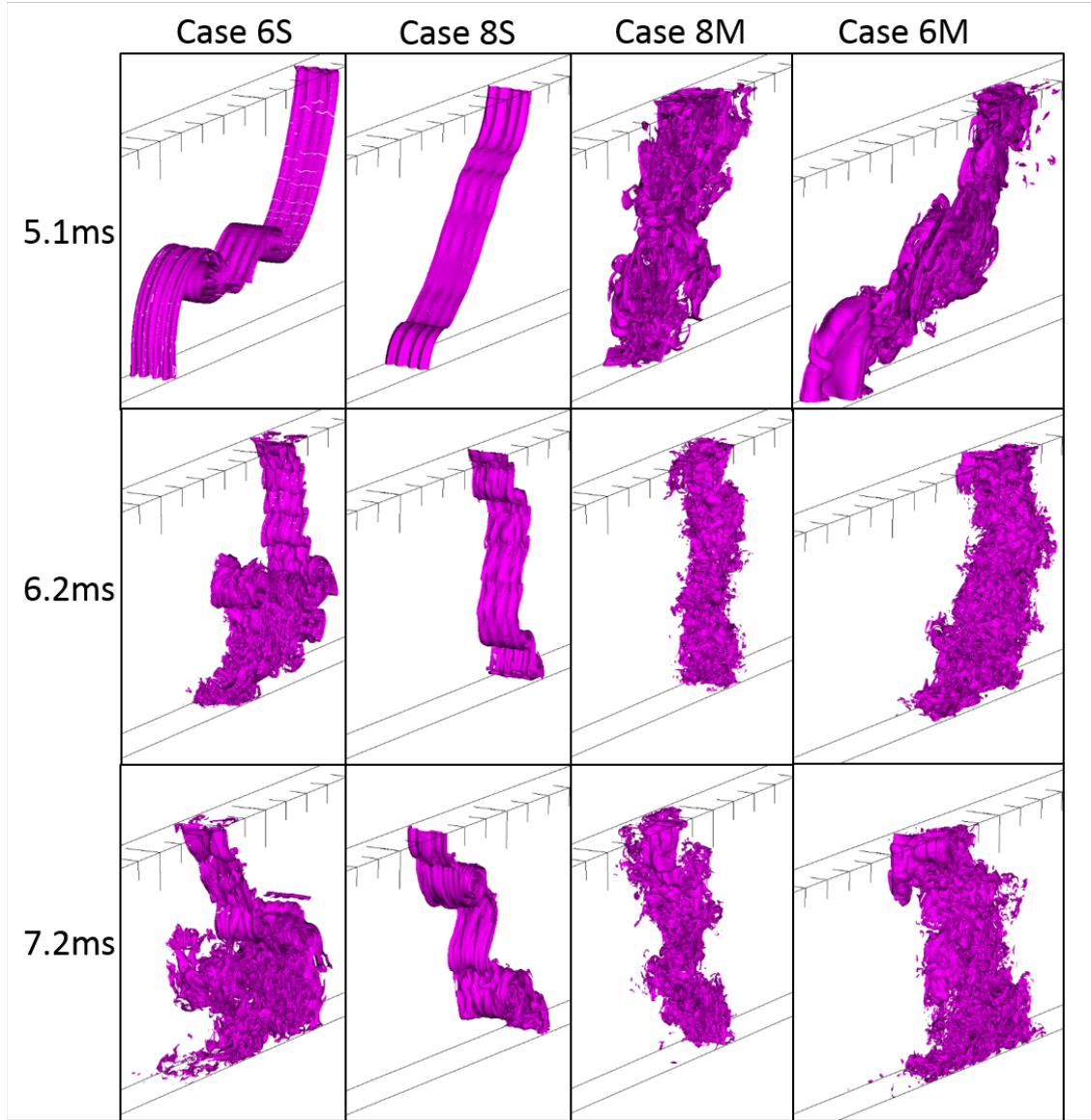


FIG. 18. (Color Online) 50% species contours of  $N_2$  for each of the four cases at three times; 5.1 ms just prior to the beginning of reshock, 6.2 ms just after the reshock, and 7.2 ms a later time after reshock.

has a similar inclination. Cases 8M and 6M have a well-mixed distribution of positive and negative vortices which are lower in magnitude than the well-organized vortices of case 6S and 8S. Case 6S shows a similar well mixed distribution of vortices in the former primary vortex region with one strong positive vortex projectile which are not present in case 8S.

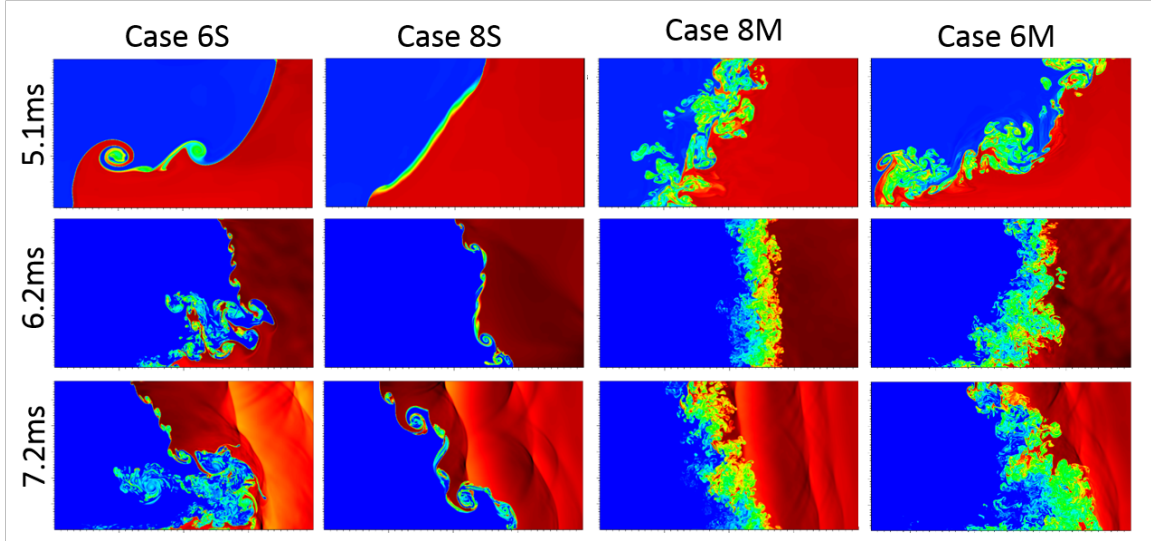


FIG. 19. (Color Online) Center slices in the X-Y plane of density. The color scales are common for all plots after reshock (6.2 ms and 7.2 ms) and before reshock (5.1 ms) .

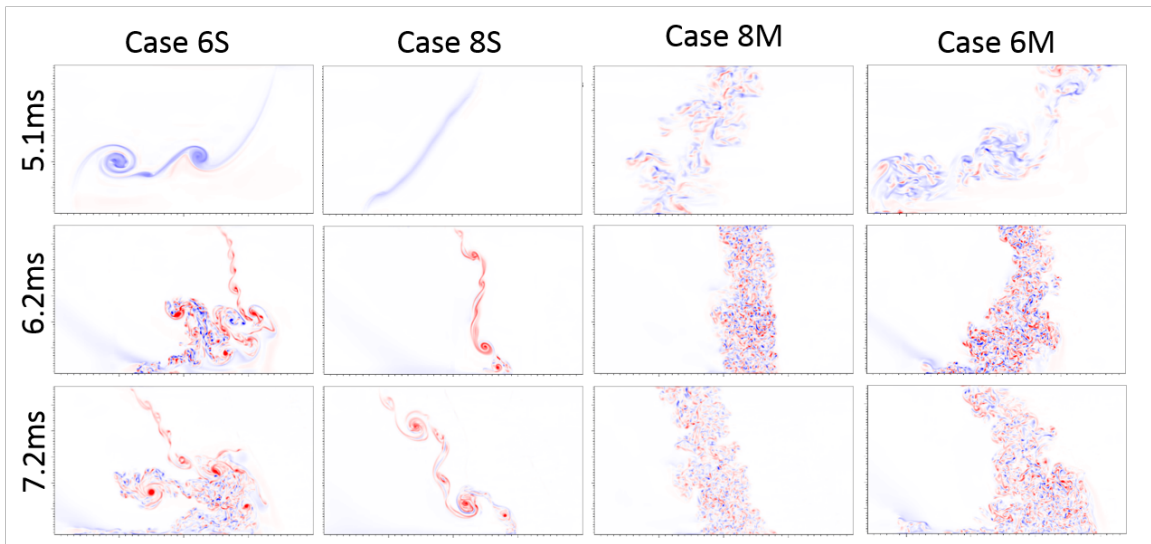


FIG. 20. (Color Online) Center slices in the X-Y plane of vorticity. The color scales are symmetric about zero and are common for all plots after reshock (6.2 ms and 7.2 ms) and before reshock (5.1 ms) .

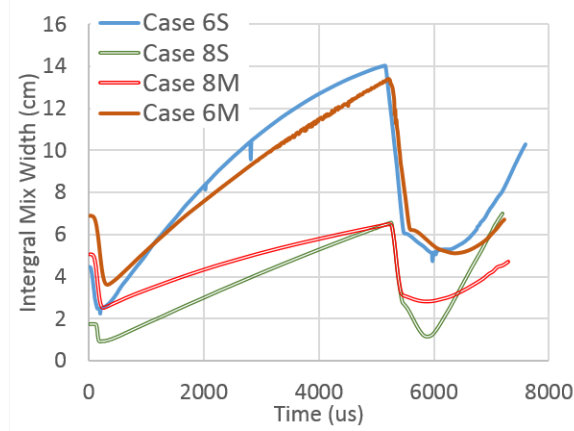


FIG. 21. (Color Online) Integral mix width over time for the four cases .

## B. Mixing measurements

The integral mix width (eqn. 23) for the four cases is shown in figure 21. The complex perturbation creates an initially larger mixing width but its larger effective diffusion thickness diminishes the energy imparted to the interface creating a slightly lower growth rate. While cases 8S and 8M have the same large wavelength amplitude, case 8S has a higher mixing width growth rate which allows it to match and even exceed case 8M just before reshock. For cases 6S and 6M with a  $60^\circ$  inclination, the higher large wavelength amplitude is less affected by the complex perturbation, and the mixing width is similar just before reshock. After reshock the growth rates of cases 6S, 8S, and 6M are similar whereas case 8M has a low growth rate due to the high effective diffusion thickness and low large wavelength perturbation amplitude. Despite the low mix width, the mixed mass (eqn. 31, fig. 22) for case 8M after reshock far exceeds that of case 8S and is similar to case 6S. The mixed mass of case 8M and 6M start out much larger than case 6S or 8S due to the complex perturbation, but unlike the mix width, the production rates are much higher before reshock compared to case 6S and 8S. The mixed mass of case 6S and 6M are increasing at a higher rate than cases 8S and 8M after reshock, and it is likely that at later times case 6S will exceed case 8M. This mixed mass in case 6S is being produced mainly in the former primary vortex region.

$$m = \frac{1}{V} \int Y_{N_2} Y_{CO_2} \rho dV. \quad (31)$$

The mixing width attempts to describe the mixing potential or large scale entrainment

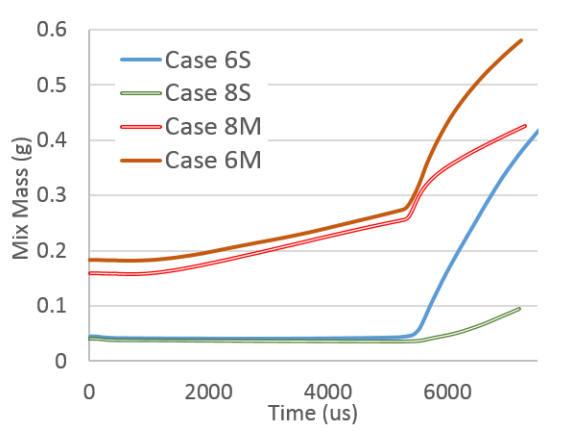


FIG. 22. (Color Online) Mixed mass over time for the four cases .

length for the interface while the mixed mass describes the amount of molecular mixing which has occurred. The mixedness [34] (eqn. 32) of the interface describes the ratio of the mixed fluid, given as the mixing length (numerator in eqn. 32), to the entrainment length or integral mix width (eqn. 3). Figure 23 shows that the mixedness for cases 8M and 6M is substantially higher in the initial conditions and remains higher for all times. Case 6S and 8S eventually converge to a similar mixedness just before reshock. After reshock the mixedness for cases 8S, 8M and 6M quickly increases as the entrainment length shrinks due to inversion and then quickly diminishes as the entrainment length grows. For case 6S after reshock the entrainment length stays larger through inversion while the primary vortex region creates a larger mixing length which persists to later times and competes with the growing entrainment length.

$$\Theta = \frac{\int_{-\infty}^{\infty} \langle Y_{N_2} Y_{CO_2} \rangle dx}{\int_{-\infty}^{\infty} \langle Y_{N_2} \rangle \langle Y_{CO_2} \rangle dx}. \quad (32)$$

Figure 23 also reveals a limitation of the mixedness parameter for the inclined interface perturbation; the initial interface entrainment length is much larger for the  $60^\circ$  interfaces though one could look at both case 6S and 8S and see that there is very little entrainment of mass which has occurred in the  $V$  direction, normal to the interface. The mixedness parameter only accounts for the total amount of each species at each  $X$  location, not how well dispersed it is. Species entrainment can be viewed as a ratio of the available surface area ( $S$ ) for diffusion to its total volume. For discrete data with a limited resolution this value will converge to a finite maximum value. This situation arises in 2D landscape data and

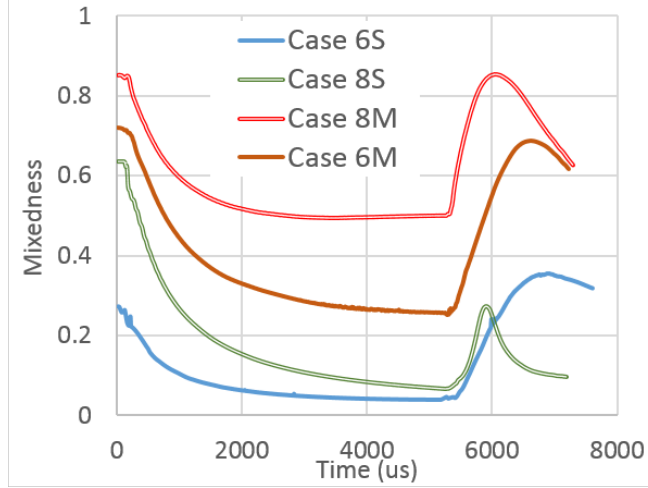


FIG. 23. (Color Online) Mixedness over time for the four cases .

has been quantified by terms such as the shape index and aggregation index [35]. In nature, entrainment has no resolution limit and would proceed to the molecular level becoming molecularly diffused. In this case the entrainment ratio would approach infinity. On the other hand, this entrainment ratio would have a finite minimum value which would be the minimum surface area ( $S_{min}$ ) possible between two continuous gas volumes. When these gas volumes are bounded by shock tube walls or a computational domain their minimum surface area becomes the cross-sectional area of the tube or computation domain ( $A = L_y L_z$ ). Using this minimum surface area, an entrainment index ( $I$  eqn. 33) was developed which has a lower bound of zero and an upper limit of one, where one would be approached as the fluids became molecularly diffused. For a simulation, the maximum resolution will limit the entrainment index to values below one and the index may decrease at late times when energy injection into the system decreases, at which point small scale structures break down and molecular diffusion takes place.

$$I = 1 - \frac{S_{min}}{S}. \quad (33)$$

For the simulation data the surface area was calculated as the area of the surface contour area of the 99% contour of  $N_2$  and  $CO_2$ . These areas differed by up to 50% as the mixing region tended to create a larger surface area for the  $N_2$ . While there is no information in this metric about the strength of gradients in these contours, one could infer that the larger  $N_2$  mass fraction contour indicates a higher diffusion rate of  $N_2$  into the mixing region. Figure

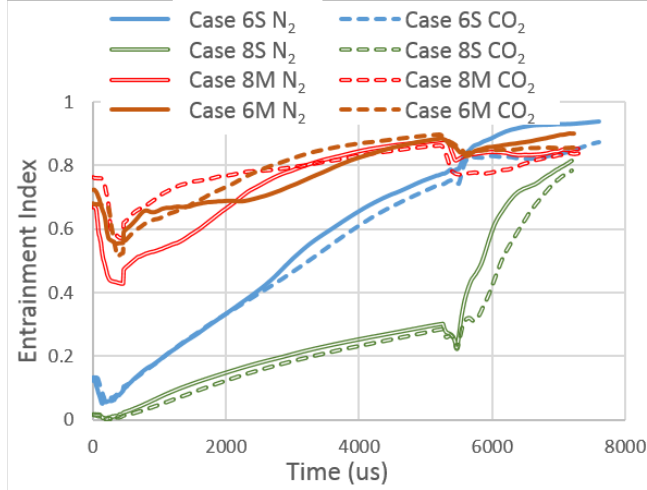


FIG. 24. (Color Online) Entrainment index over time for the four cases .

24 shows the entrainment index for each case and species over time. At early times cases 6M and 8M possess the highest entrainment index. One might expect that case 6M would have a greater entrainment index than case 8M due to its longer inclined interface length, but there is some amount of variation in the initial contours created by the complex stratification (section III A), and as the entrainment index becomes larger it becomes less sensitive to the differences in the interface surface area. The incident shock and reshock compress the surface area of the interface and therefore the entrainment index. The entrainment index of cases 8M and 6M increases slowly until reshock, while case 6S increases much faster. After reshock the mixing width for case 6S and 6M remains larger through reshock compression and then expands again allowing the entrainment index to compress only slightly with reshock and then to grow beyond case 8M. The small pockets of mass created from the remnants of the primary vortex exhibit less diffusion and a large 99% contour surface area compared to the turbulent mixing layer of the complex stratification cases. Case 8S exhibits the largest growth in entrainment index after reshock and becomes nearly equal to case 8M. Again, case 8S has a sharper species gradient and less diffusion which allows the surface area to grow much faster. The difference in species entrainment index for case 8M at early times suggests a stronger diffusion of  $CO_2$  into the mixing region at early times. This is an artifact of the complex stratification initial conditions. At later times all cases exhibit a higher  $N_2$  surface area.

Taking advantage of the fact that the inclined interface perturbation has only a half large

wavelength perturbation in the computational domain it is possible to estimate the secondary entrainment by separating out the large scale structure of the inclined interface. An effective inclined interface height ( $h_E$ ) can be created at all times by replacing the mixing interface with an ideal inclined interface, with no mixing, at all times which creates the same integral mix width. Through some calculus it can be shown that the height (X dimension length) of this effective interface would be three halves the integral mix width. Using this height, and the Y and Z dimension of the computational domain (11.43 cm and 2.286 cm), we can find the hypotenuse and surface area of this effective inclined interface ( $S_E$ ). An estimate of the secondary entrainment created by features which are not driven by the linear growth of the large wavelength perturbation can be made by taking the ratio of the contour surface area to the effective inclined interface surface area (eqn. 34). This secondary entrainment ratio ( $R$ ) can increase due to non-linear features such as the primary and secondary vortices as in case 6S or due to secondary perturbations or 3D features. In figure 25 it can be seen that case 8M starts with a relatively high  $R$  followed by case 6M and that both grow steadily after the incident shock interaction. Case 6S and 8S start with  $R$  very close to one. Only after the primary and secondary vortices begins to grow and entrain fluid does  $R$  for case 6S increase significantly while case 8S stays small until reshock. After reshock the  $R$  for case 6S and 6M increase sharply with the  $N_2$   $R$  increasing far beyond the  $CO_2$   $R$ . The difference in the contour surface areas for  $N_2$  and  $CO_2$  in case 6S is due largely to the remnants of the primary vortex which entrain mixed mass, and do not contain a 99%  $CO_2$  contour, into pure  $N_2$ . Case 6S can be seen to have a higher average  $R$  after reshock than case 8M, or 6M even, suggesting that the simple high-amplitude large-wavelength perturbation creates a higher entrainment with reshock. Case 8Ss  $R$  also increases significantly and becomes comparable to case 8M.

$$R = \frac{S}{S_E} = \frac{S}{\sqrt{(1.5h)^2 + L_Y^2 * L_Z^2}}. \quad (34)$$

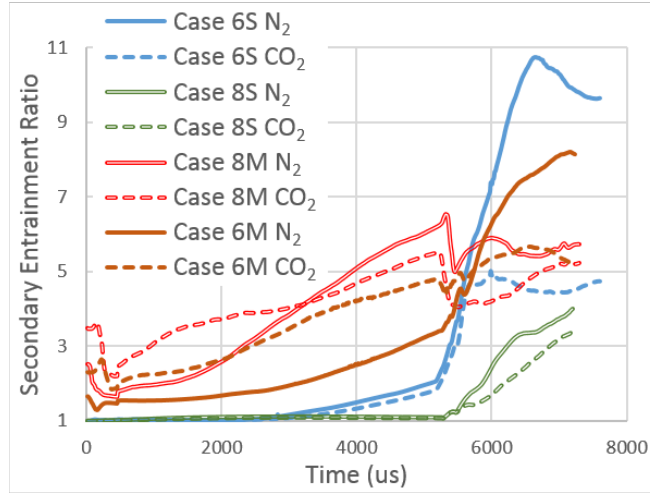


FIG. 25. (Color Online) Secondary Entrainment Ratio ( $R$ ) for the four cases over time .

### C. Vorticity measurements

The enstrophy plot (fig. 26) for the four cases shows that the complex multimode cases have nearly equal enstrophy after reshock and that they are the highest of the cases. The enstrophy for case 8M peaks earlier and decays faster as the reshock wave passes through the shorter pre-reshock interface faster. Case 6S has a high enstrophy as well but it does not reach the levels of the complex multimode cases. The circulation components (X, Y, and Z positive, negative, and total) for each of the four cases is shown in figure 27. The Z circulation for all cases is the largest as the inclined interface perturbation dominates the vorticity field even for case 8M. The inclined interface alone creates an initial negative vorticity from the incident shock which reverses sign after reshock. For both these cases the Z circulation remains strong after reshock while the X and Y circulation is initially amplified and decays quickly. The Y vorticity is initially damped by a larger effective diffusion layer in the X-Z plane and grows slower and persists longer after reshock. For case 8M, the Z vorticity is initially larger but of a similar magnitude to case 6S; however, the X and Y components are larger due to the complex perturbation. After reshock the vorticity is amplified but quickly decays for case 8M and 6M, though case 6M persists a bit longer. This is due to the well distributed smaller scale features which are dissipating energy much more quickly than case 6S or 8S. Case 6M persists longer due to the large amplitude long wavelength perturbation which is able to recover some additional circulation at late times. The decay rate of case 8M is asymptoting to a constant value which may be reached if the simulations were run longer without addition accelerations from the spurious expansion waves.

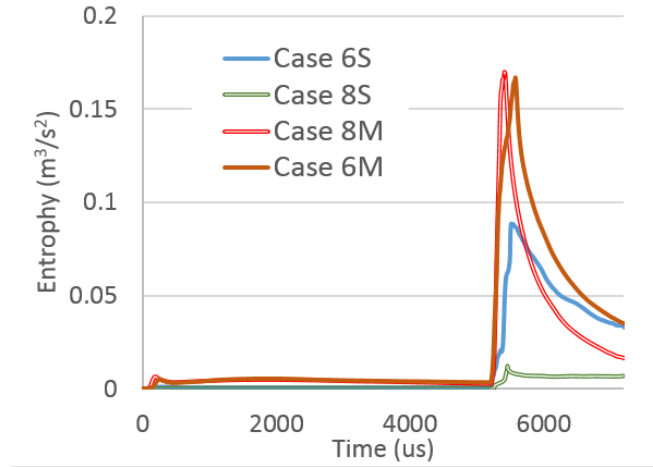


FIG. 26. (Color Online) Entropy over time for the four cases .

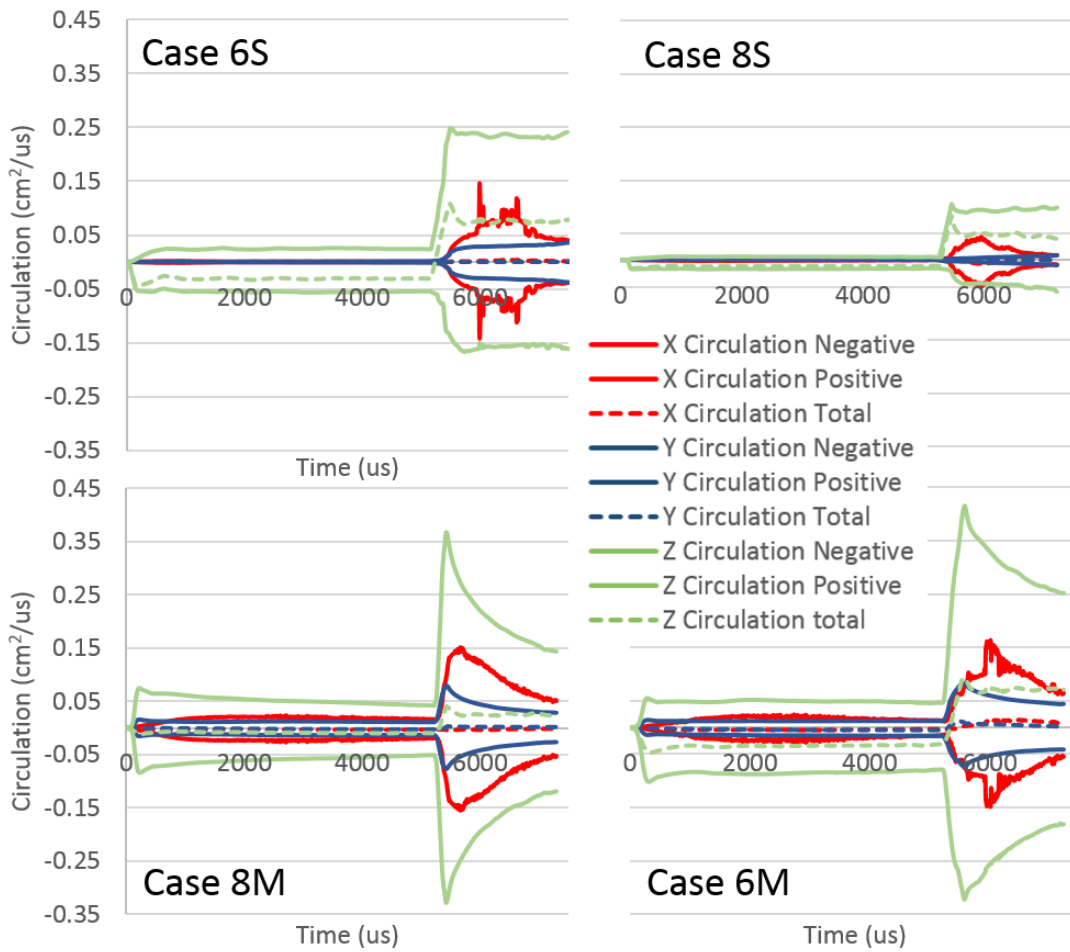


FIG. 27. (Color Online) Circulation components over time for the four cases .

#### D. Turbulence quantities

To find spatially varying quantities the AMR data was first resampled to the highest level resolution over the mixing region. The fluctuating velocity fields of the four cases were found using Favre averaging over the Y-Z planes (eqns. 35 and 36). The turbulent kinetic energy (TKE) was found using these fluctuating velocities before (5.1ms) and after reshock (6.2, 6.7, and 7.2 ms). The spectra was found using the 2D Fourier transform of the TKE at each Y-Z plane and then averaged over the X direction. Since the inclined interface provides a strong 2D perturbation the 1D spectra were found for the  $K_y$  and  $K_z$  directions by averaging over the 2D Fourier data over the  $K_z$  and  $K_y$  directions, respectively. Figures 28 and 29 show the TKE spectra over the  $K_y$  and  $K_z$  wave numbers. It is immediately apparent that the simulations have a limited effective resolution of about 2.5 mm where the inertial range breaks and a strong dissipation range is created by unresolved scales. Before reshock cases 6S and 8S have not developed an inertial range while cases 8M and 6M have. Case 6M still has a higher energy at low wave numbers from the high amplitude  $60^\circ$  large wavelength perturbation. After reshock case 8S shows an inertial range which is more limited compared to cases 6S, 8M, and 6M. Among these cases there is very little distinction between their TKE spectra. Only at the lowest wave numbers can it be seen that case 8M possesses a lower energy at the smallest wave numbers, even smaller than case 8S which shares its initial large wavelength perturbation amplitude. Case 8M's large wavelength perturbation was damped out by reshock as it had a small amplitude before reshock and a large degree of mixing which damped the vorticity deposition by reshock.

$$\bar{u}_i = \frac{\langle \rho u_i \rangle}{\langle \rho \rangle}. \quad (35)$$

$$u'_i = u_i - \bar{u}_i. \quad (36)$$

The plot of TKE for the Z spectra (fig. 29) shows that a limited inertial range develops in this direction but that the large wavelength Z inclination perturbation persists for cases 6S and 8S to late time and possesses the largest amount of energy. The complex stratification cases have a smoother distribution of energy before reshock and after reshock cases 6S, 8M, and 6M possess a similar amount of energy across most of the small wave numbers. At the

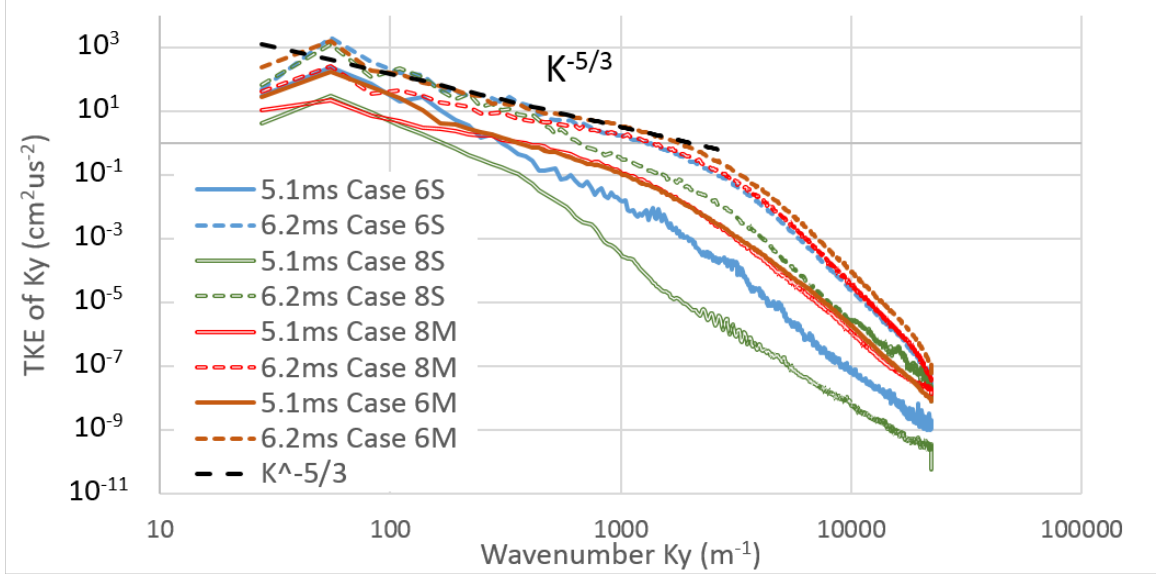


FIG. 28. (Color Online) Turbulent kinetic energy of the  $K_y$  wave numbers .

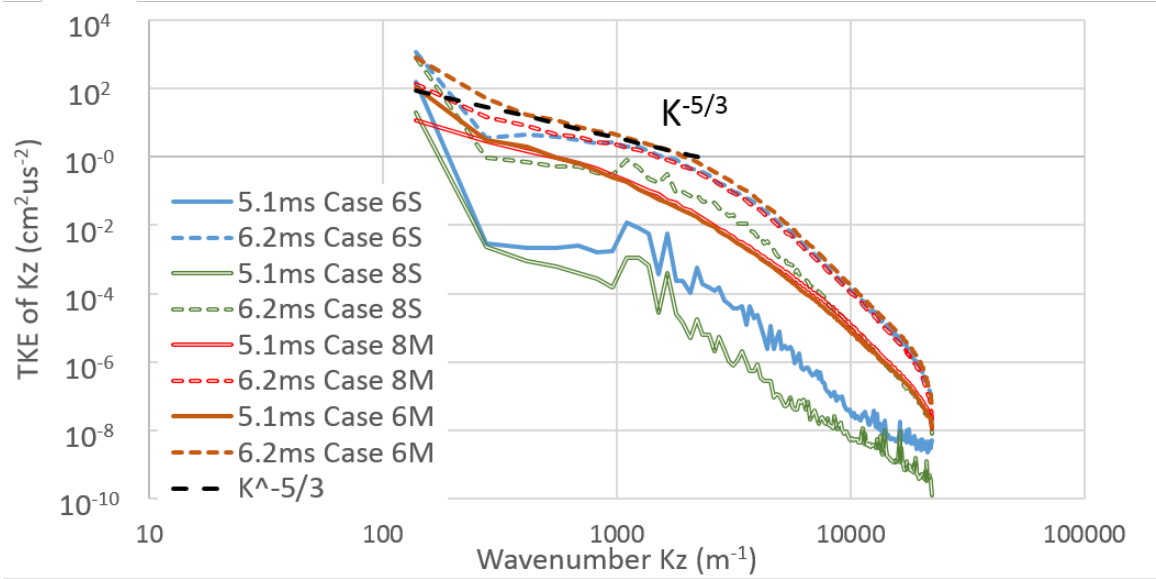


FIG. 29. (Color Online) Turbulent kinetic energy of the  $K_z$  wave numbers .

lowest wave number all cases possess a higher amount of energy due to the memory of the initial small amplitude large wavelength perturbation.

The density self-correlation,  $b$ , (eqn. 37) is an important parameter for turbulence modelling using second-moment models for variable-density flows which are beyond the Boussinesq approximation, which include RM and RT turbulence [5]. This parameter appears in the turbulent mass flux equation (eqn. 38) as a coefficient in the production term. The  $b$

parameter goes to zero as the fluid becomes perfectly mixed and is unbounded as the fluid densities diverge and the material becomes completely unmixed [36]. Figure 30 shows the  $b$  parameter over the mixing layer for the four cases before and at early times after reshock. After reshock the  $b$  parameter decays steadily as the flow becomes well mixed. The two center peaks in case 6S before reshock come from the two vortices that form while the outer peaks are formed by the steep interface edges, which align with the averaging plane, and the weak 3D perturbation. For cases 6S, 8M, and 6M the  $b$  parameter is higher before reshock. For case 8S the  $b$  parameter increases after reshock as the flow becomes turbulent. The pre-reshock magnitudes for cases 6S and 8S are very similar differing only in spatial distribution while case 6M exhibits a similar distribution to case 6S with a slightly diminished magnitude and no peak at the upstream edge. Case 8M has a much lower density self-correlation value at both times due to its larger more diffuse mixing layer and lower inclination amplitude which grows slowly producing little stretching or steep species gradients. Most of the maximum values of the density self-correlation appear near the center as there is only a single interface.

$$b = \langle -\rho'(1/\rho)' \rangle. \quad (37)$$

$$a_i = \frac{\overline{\rho' u_i'}}{\bar{\rho}}. \quad (38)$$

The anisotropy of the flow provides insight into the memory of the 2D initial inclined interface perturbation. The magnitude of the deviatoric anisotropy tensor provides a measure of the anisotropy as a function of  $X$  location for the four cases (eqns. 39 and 40). Cases 6S and 6M, the  $60^\circ$  inclination cases, possess a significant anisotropy before reshock while cases 8S, and 8M are mostly isotropic (fig. 31). Case 6S has the highest anisotropy in the primary vortex region ( $X$  -4 cm). All cases exhibit an increased anisotropy after reshock though case 8M is significantly lower than the other cases. Cases 6S and 6M, exhibit the highest anisotropy but case 6S possesses a peak in the upstream flow field driven by remnants of the mostly 2D primary vortex. As a fraction of the turbulent kinetic energy (eqn. 41), the anisotropy between the cases is much more similar (fig. 32). Case 6S before reshock stands out by this measure as having a high normalized anisotropy while case 8M has the lowest normalized anisotropy at both times.

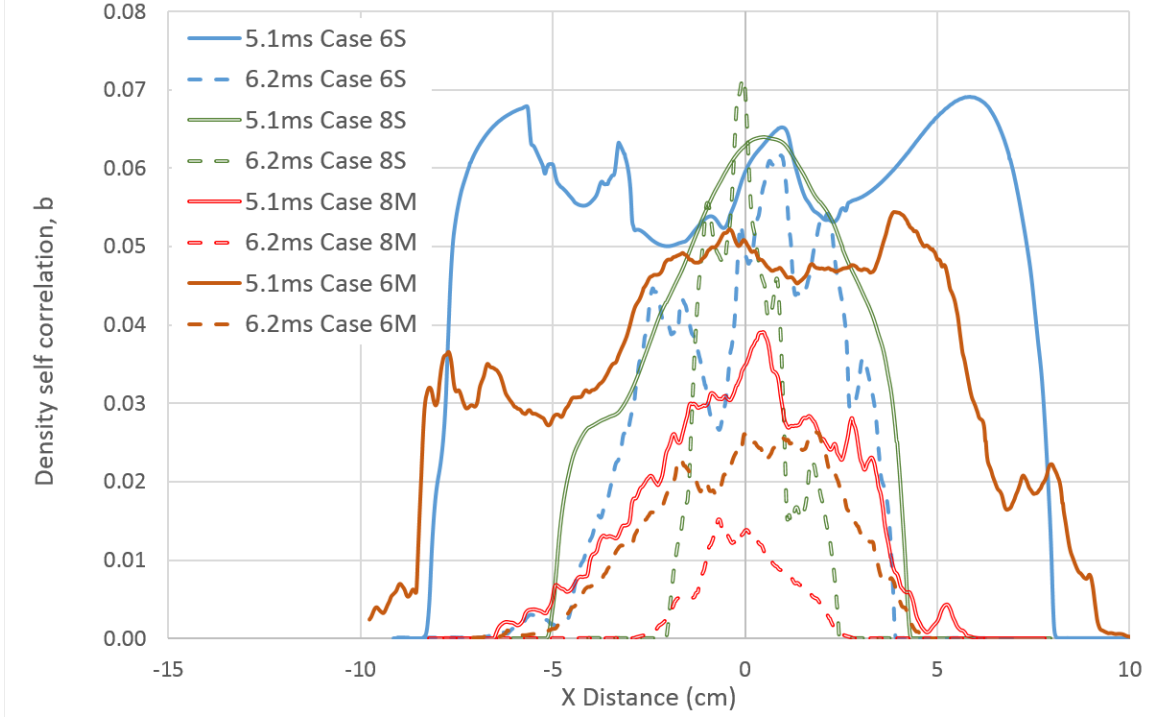


FIG. 30. (Color Online) Density self-correlation ( $b$ ) for the four cases before (5.1 ms) and after reshock (6.2 ms) .

$$a_{ij}(x) = \langle u'_i(x)u'_j(x) \rangle - \frac{1}{3}\langle u'_k(x)u'_k(x) \rangle \delta_{ij}. \quad (39)$$

$$\|a(x)\| = \sqrt{a_{ij}(x)a_{ij}(x)}. \quad (40)$$

$$\|\beta\| = \frac{a_{ij}(x)a_{ij}(x)}{\langle u'_k(x)u'_k(x) \rangle}. \quad (41)$$

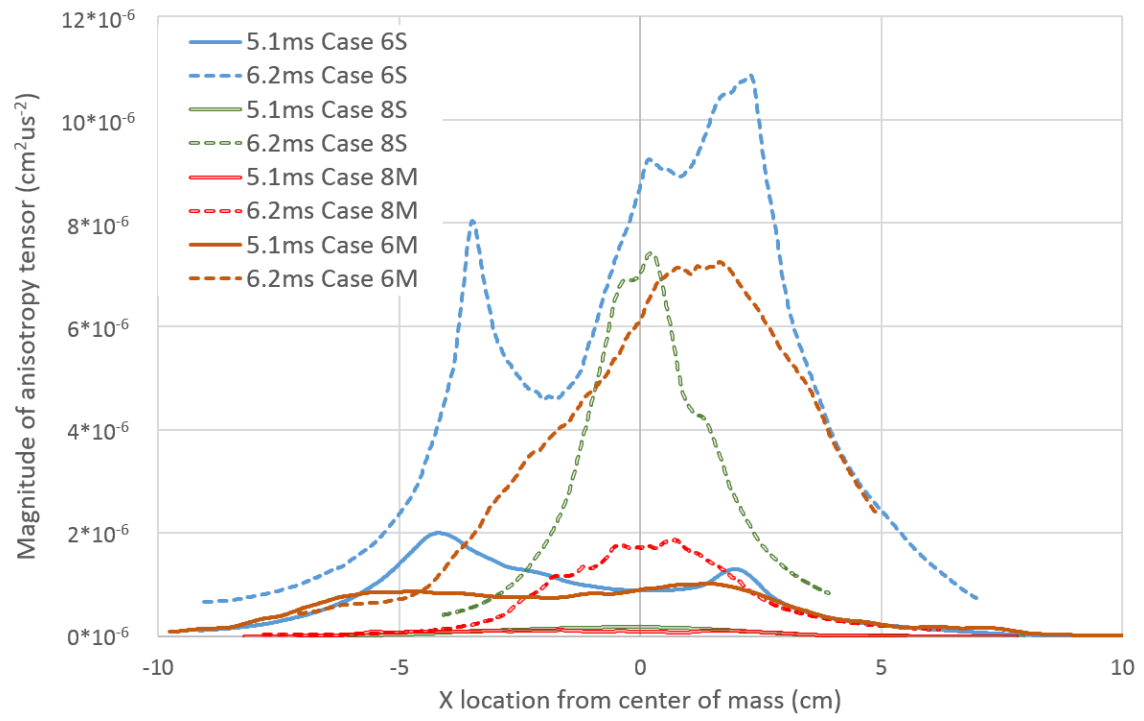


FIG. 31. (Color Online) Magnitude of the deviatoric anisotropy tensor for the four cases before (5.1 ms) and after reshock (6.2 ms) .

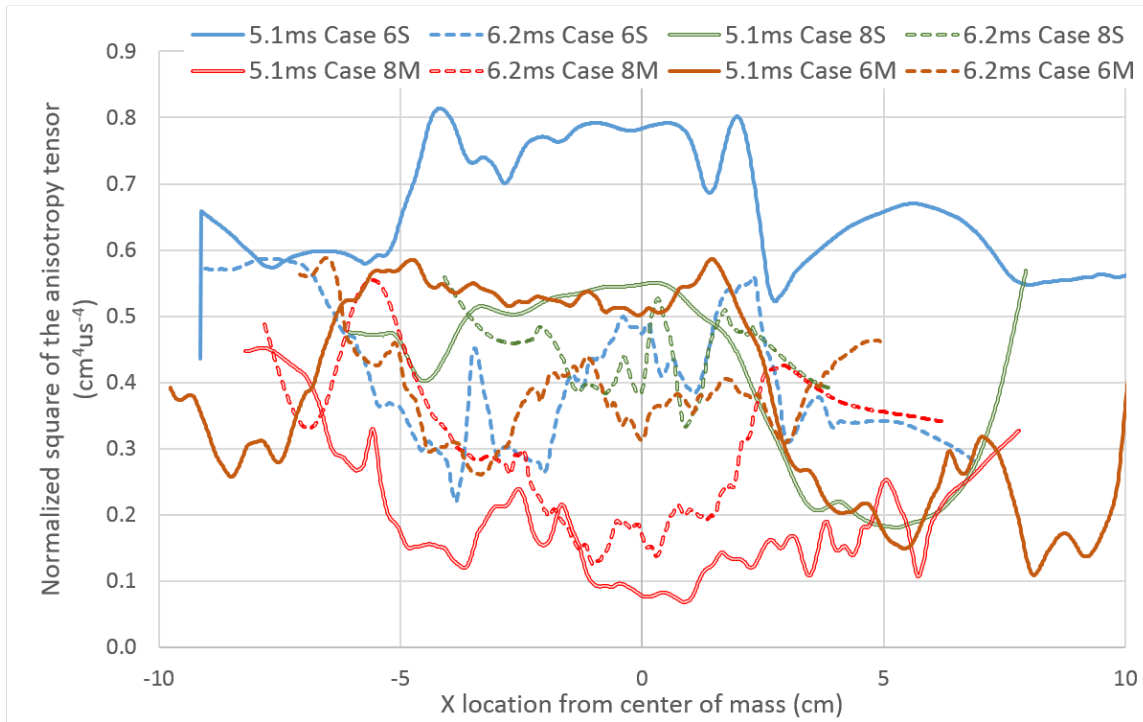


FIG. 32. (Color Online) Normalized square of the deviatoric anisotropy tensor for the four cases before (5.1 ms) and after reshock (6.2 ms) .

#### IV. CONCLUSIONS

The results of this simulation study highlight the effect of a large wavelength single mode perturbation, created by the inclined interface, on the mixing created by small wavelength multimode perturbations. A summary of the major conclusions from this work are listed below.

- Before reshock mixing is driven by the small wavelength multimode perturbations while large scale measures such as the mix width are driven by the large wavelength perturbation. This division of attributes is not clear after reshock.
- After reshock the simple nonlinear large wavelength perturbation generates small scale mixing similar to the small wavelength multimode perturbations suggesting a loss of memory of the initial perturbation wavelength.
- After reshock the small scale multimode perturbations suppress large scale measures of the linear large wavelength perturbation but not of the nonlinear large wavelength perturbation. This suggests that the late time turbulence has a memory of the linearity (amplitude) of the large wavelength perturbation.

Before reshock the simple inclined interface cases (6S and 8S) and the multimode complex stratification cases (8M and 6M) exhibit distinct traits which identify their initial conditions. Small scale mixing measurements such as mix mass, entrainment, and TKE spectra show case 6S and 8S are markedly different from cases 8M and 6M. Cases 6S and 8S process low mixing and entrainment and have poorly developed inertial ranges in their TKE cascades. Large scale driven measures such as the mix width and turbulent anisotropy are dominated by the large wavelength perturbation amplitude and group cases 6S and 6M together. The integral mix width is dominated by the growth of the large wavelength perturbation before reshock and leads to the development of a large shear layer which increases the anisotropy. The simple nonlinear large wavelength perturbation (case 6S) generates secondary mixing features before reshock in the primary vortex region. While this mixing is small compared to that exhibited by the small wavelength multimode perturbations it is greatly amplified by the reshock process. After reshock case 6S exhibits mixing measures which are similar to cases 8M and 6M. The turbulent kinetic energy spectra exhibits a well-defined inertial range, and high amount of circulation similar in magnitude to cases 8M and 6M. Case 6S

also displays a large entrainment index and mix mass which are nearly identical to the small wavelength multimode perturbation cases. The normalized anisotropy of case 6S also drops significantly after reshock becoming similar to the other cases. By mixing and circulation measures the simple nonlinear large wavelength perturbation has little memory of the small wavelength perturbations or complexity of its initial conditions. For case 8M, linear large wavelength perturbation coupled with the small amplitude multimode perturbation, memory of the large wavelength perturbation initial conditions is apparently lost. Case 8M exhibits the most turbulent like measures having the lowest anisotropy, density self-correlation, and mix width, while possessing a well formed inertial range and a high degree of entrainment and mixed mass. Case 8M also has the lowest mix width and entrainment growth rates, as well as the highest circulation dissipation rate. In contrast case 6M, nonlinear large wavelength and small amplitude multimode perturbation, shows a distinct memory of its initial conditions in large scales measures such as a large mix width, high anisotropy, and persisting circulation in the Z direction. The nonlinear large wavelength perturbation drives the complex multimode case to be less isotropic and to retain a memory of the initial conditions in large scale measures.

## ACKNOWLEDGMENTS

The simulation images in this paper were created using the program VisIt [37] and the authors would like to thank the VisIt developers for their support of this program. The authors would also like to acknowledge the support Lawrence Livermore National Laboratory (LLNL) for providing the computing time for the simulations presented in this work. JM would like to thank Britton Olson and Oleg Schilling of LLNL for their consultation and advice. DR would like to acknowledge the support of National Science Foundation Faculty Early Career Development (CAREER) Award (Grant No. CBET-1451994), and the Air Force Office of Scientific Research Young investigator Award (Grant number FA9550-13-1-0185).

- 
- [1] Y. A. Kucherenko, A. V. Pavlenko, O. E. Shestachenko, S. I. Balabin, A. P. Pylaev, and A. A. Tyaktev, *Journal of Applied Mechanics and Technical Physics* **51**, 299 (2010).

- [2] G. Bouzgarrou, Y. Bury, S. Jamme, L. Joly, and J.-F. Haas, *Journal of Fluids Engineering* **136**, 091209 (2014).
- [3] L. Erez, O. Sadot, D. Oron, G. Erez, L. A. Levin, D. Shvarts, and G. Ben-Dor, *Shock Waves* **10**, 241 (2000).
- [4] D. Ranjan, J. Niederhaus, B. Motl, M. Anderson, J. Oakley, and R. Bonazza, *Physical Review Letters* **98**, 024502 (2007).
- [5] C. D. Tomkins, B. J. Balakumar, G. Orlicz, K. P. Prestridge, and J. R. Ristorcelli, *Journal of Fluid Mechanics* **735**, 288 (2013).
- [6] B. Motl, J. Oakley, D. Ranjan, C. Weber, M. Anderson, and R. Bonazza, *Physics of Fluids* **21**, 126102 (2009).
- [7] V. V. Krivets, C. C. Long, J. W. Jacobs, and J. A. Greenough, in *26th International Symposium on Shock Waves*, Vol. 2 (Springer, Gottingen, Germany, 2009) pp. 1205–1210.
- [8] P. R. Chapman and J. W. Jacobs, *Physics of Fluids* **18**, 074101 (2006).
- [9] H. F. Robey, J. O. Kane, B. A. Remington, R. P. Drake, O. A. Hurricane, H. Louis, R. J. Wallace, J. Knauer, P. Keiter, D. Arnett, and D. D. Ryutov, *Physics of Plasmas* **8**, 2446 (2001).
- [10] M. Latini, O. Schilling, and W. S. Don, *Physics of Fluids* **19**, 024104 (2007).
- [11] G. Peng, N. J. Zabusky, and S. Zhang, *Physics of Fluids* **15**, 3730 (2003).
- [12] M. Lombardini, D. I. Pullin, and D. I. Meiron, *Journal of Fluid Mechanics* **690**, 203 (2012).
- [13] F. F. Grinstein, A. A. Gowardhan, and A. J. Wachtor, *Physics of Fluids* **23**, 034106 (2011).
- [14] B. J. Olson and J. Greenough, *Physics of Fluids* **26**, 044103 (2014).
- [15] A. R. Miles, B. Blue, M. J. Edwards, J. A. Greenough, J. F. Hansen, H. F. Robey, R. P. Drake, C. Kuranz, and D. R. Leibbrandt, *Physics of Plasmas* **12**, 056317 (2005).
- [16] J. Kane, R. P. Drake, and B. A. Remington, *The Astrophysical Journal* **511**, 335 (1999).
- [17] G. Taylor, *Proceedings of the Royal Society of London. Series A, Mathematical and Physical Sciences* **201**, 192 (1950).
- [18] J. Rayleigh, *Proceedings of the London Mathematical Society* **14**, 170 (1883).
- [19] J. McFarland, D. Reilly, S. Creel, C. McDonald, T. Finn, and D. Ranjan, *Experiments in Fluids* **55** (2013), 10.1007/s00348-013-1640-1.
- [20] C. Weber, N. Haehn, J. Oakley, D. Rothamer, and R. Bonazza, *Physics of Fluids* **24**, 074105 (2012).

- [21] R. Mejia-Alvarez, B. Wilson, and K. P. Prestridge, in *Bulletin of the American Physical Society*, 20, Vol. 59 (San Francisco, Ca, 2014).
- [22] D. Reilly, J. A. McFarland, and D. Ranjan, *Experiments in Fluids* **In review** (2015).
- [23] M. L. Wilkins, *Calculation of Elastic Plastic Flow*, Tech. Rep. UCRL-7322 (University of California Lawrence Radiation Laboratory, 1963).
- [24] T. V. Kolev and R. N. Rieben, *Journal of Computational Physics* **228**, 8336 (2009).
- [25] R. W. Sharp and R. T. Barton, *HEMP Advection Model*, Tech. Rep. UCID-17809 (Lawrence Livermore Laboratory, 1981).
- [26] M. J. Berger and J. Olinger, *Journal of computational Physics* **53**, 484 (1984).
- [27] M. J. Berger and P. Colella, *Journal of computational Physics* **82**, 64 (1989).
- [28] A. W. Cook, *Physics of Fluids* **21**, 055109 (2009).
- [29] J. McFarland, J. Greenough, and D. Ranjan, *Physical Review E* **84**, 026303 (2011).
- [30] J. A. McFarland, J. A. Greenough, and D. Ranjan, *Journal of Fluids Engineering* **136**, 071203 (2014).
- [31] E. R. Gilliland, *Industrial and Engineering Chemistry* **26**, 681 (1934).
- [32] B. Poling, J. Prausnitz, and J. O’Connell, *The Properties of Gases and Liquids*, 5th ed. (McGraw-Hill, 2000).
- [33] R. V. Morgan, R. Aure, J. D. Stockero, J. A. Greenough, W. Cabot, O. A. Likhachev, and J. W. Jacobs, *Journal of Fluid Mechanics* **712**, 354 (2012).
- [34] W. H. Cabot and A. W. Cook, *Nature Physics* **2**, 562 (2006).
- [35] H. S. He, B. E. DeZonia, and D. J. Mladenoff, *Landscape Ecology* **15**, 591 (2000).
- [36] J. D. Schwarzkopf, D. Livescu, R. A. Gore, R. M. Rauenzahn, and J. R. Ristorcelli, *Journal of Turbulence* **12**, N49 (2011).
- [37] H. Childs, E. Brugger, B. Whitlock, J. Meredith, S. Ahern, D. Pugmire, K. Biagas, M. Miller, C. Harrison, G. H. Weber, H. Krishnan, T. Fogal, A. Sanderson, C. Garth, E. W. Bethel, D. Camp, O. Rübel, M. Durant, J. M. Favre, and P. Navrátil, in *High Performance Visualization—Enabling Extreme-Scale Scientific Insight* (2012) pp. 357–372.